Chapter 6

Formation of High Valent Metal-oxo Species (Oxo Wall)

6.1 Introduction

High valent metal-oxo species are reactive key intermediates in many processes; such as catalytic oxidation of the organic substrate, water by many enzymes, and biomimetic compounds.[1-8] These species such as iron/manganese-oxo also act as an oxidizing intermediate in many biological oxidation reactions such as respiration, metabolism, and photosynthesis.[9-21] A terminal metal-oxo is often invoked as the primary product of O-O bond cleavage of the ORR (oxygen reducatse reaction) and conversely, O-O bond formation of the OER (oxygen evolving reaction) is often proposed to proceed from a high valent metal-oxo species.[22-23] Manganese-oxo species are involved in the oxygen-evolving complex (OEC) in the photosystem-II, catalase, and manganese superoxide dismutase.[24] Heme iron-oxos are found in P450, cytochrome c oxidase, and the terminal enzyme in respiration. High valent iron(IV)-oxo complexes are the oxidizing agent in the catalytic cycle of tyrosine hydroxylase, and aliphatic halogenase SyrB2.[12] Therefore, the chemistry of high valent terminal metal-oxo species in early transition metals is well known. Early, transition metal forms stable high valent metal-oxo complexes because of the strong π-electron donor nature of terminal oxo ligand and metal have empty *d* orbitals due to which π bond formation takes place by *dπ-pπ* bonding.[25-27] Many terminal metal-oxo species of, chromium,[28] manganese,[29-33,] and iron[34-39] have been synthesized, isolated, and characterized successfully. These species involve in many reactions such as C-H bond activation, and oxygen atom transfer reactions of metalloenzymes, which help to develope oxidizing catalysts.[40-41]

However, synthesis and characterization of high valent terminal metal-oxo species of late transition metals such as cobalt, nickel, and copper remained a long-standing challenge due to an existing strong electronic repulsion between *d* orbital of metals and *p* orbital of oxo due to high *d*-electron count. In oxo species, bond order also decreases due to occupancy of M-O π antibonding orbital due to which late transition metal-oxo species are not stable.[26] Terminal

metal-oxo species are formed by O-O bond cleavage of the ORR (oxygen reductase reaction).[42-48] It may occur either by homolytic or heterolytic cleavage of O-O bond depends upon the electronic environment, i.e. electron-rich environment favors homolytic cleavage, while an electron-deficient environment favors heterolytic cleavage. The formation of terminal oxo is also related to the concept of Oxo wall which is given by Gray and Winkler.[49-50] According to Gray and Winkler, "terminal metal-oxo is not supported by the transition metals beyond eight group metals in tetragonal geometry".

Cr	Mn	Fe	Co	Ni	Cu
Mo	Tc	Ru	Ir	Pd	Ag
W	Re	Os	Rh	Pt	Au

Scheme 6.1. A representation of the "Oxo wall".

Although the metal-oxo species beyond group 8 can be stabilized by using the Lewis acid which can also stabilize the metal-oxo by combining with oxygen.[48]

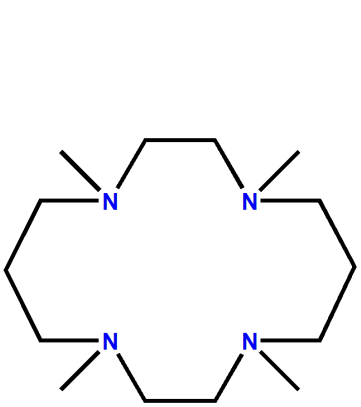

14-TMC

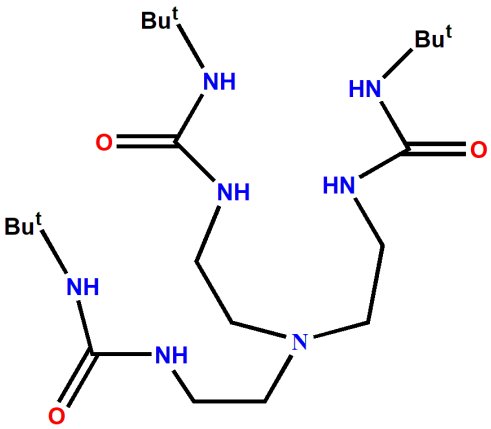

buea

Scheme 6.2. 14-TMC and buea ligand.

Considering all above points, here first time we have undertaken the computational study based on computations of transition states to specifically address the following issues; to find out the reason behind the formation of Oxo wall, by computing and comparing electronic structures of metal hydroperoxo and metal-oxo of first transition series (Cr-Cu) with two different ligands 14-TMC[49] and buea,[50-53] because of the presence of many metal-TMC/buea species, and TMC ligand with octahedral geometry while the buea have trigonal bipyramidal geometry and forms cavity like oxo species. Computing barrier height of O---O bond cleavage and the energetics of the metal-oxo species, followed by a comparative study among them.

6.2 Computational Details

Gaussian16 program is used for all the calculations.[54] Fragment approach is present in Gaussian16, used for all the spin state calculations. Based on previous work, it is predicted that B3LYP,[55-56] B3LYP-D2,[57] wB97XD[58] are advocated to find the correct spin as the ground state of reactant, intermediate, and product. B3LYP-D2 is most appropriate among these.[59-62] So here, we have restricted our calculations only to B3LYP-D2 functional, incorporating dispersion correction of Grimme *et al.*[63-65] The basis set LACVP comprises LanL2DZ-Los Alamos effective core potential for the metals (V, Cr, Mn, Fe, Co, Ni, and Cu)[66-67], and 6-31G/6-31G* basis set is for other atoms (hydrogen, carbon, nitrogen, oxygen, and chlorine) has been used.[68] TZVP basis set is used for all atoms on the optimized geometries for the single point energy calculation.[69-70] Wiberg bond indices are computed by using the natural atomic orbital analysis (NBO). NBO and SNO (spin natural orbital) are performed using G16. Solvation energies are computed by the PCM model using acetonitrile (with TMC ligated species) and n,n-dimethyl amide (with buea ligated species) as a solvent. The transition state is verified by a single negative frequency, animating the corresponding

frequency, and visualized in Gauss View. DFT energies are quoted using B3LYP-D2 solvation including free-energy corrections at 298.15 K temperature. Common notation of $^{mult}MX_{spinstate}$-Y is used throughout, where mult denotes total multiplicity, M represents metal (I=Cr, II=Mn, III=Fe, IV=Co, V=Ni, VI= Cu), and X to ligand (A for the TMC-14, and B for buea), spin state denote the possible spin states and Y represents the transition state and intermediate.

6.3 Results and Discussion

Based on earlier theoretical and experimental studies,[59-61] we have proposed a mechanism for the generation of metal-oxo (such as M^{IV}-oxo and the M^{V}-oxo) from the metal hydroperoxo species is shown in Scheme 6.3. This mechanism is based on O---O bond cleavage, where homolytic cleavage gives the M^{IV}oxo species and the heterolytic cleavage gives M^{V}oxo species. Here, we have computed the structure of 3*d* transition metal hydroperoxo (chromium to copper) species, barrier heights of the O---O bond cleavage, structure, and energetic of the metal-oxo species. We have started calculations with species IA (Cr^{III}-OOH).

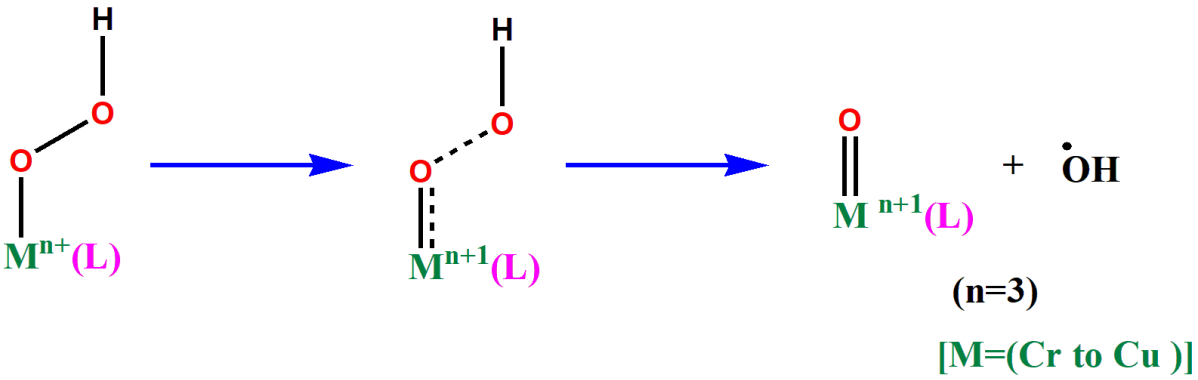

Scheme 6.3. Proposed mechanism for the formation of metal-oxo species.

6.3.1 Metal hydroperoxo species (chromium (IA), manganese (IIA), iron (IIIA), cobalt (IVA), nickel (VA), and copper (VIA))

We have optimized all possible spin states of species IA (Cr^{III}-OOH) and our results show that the $^{4}IA_{hs}$ is found as the ground state and $^{2}IA_{ls}$ is 157.0 kJ/mol higher in energy (see Figure 6.1).[60] Selected bond parameters are shown in Table AX 6.1 of appendix and spin density plots are shown in Table 6.1. Spin density plot and optimized structure of the ground state are shown in Figure 6.1 and Figure 6.2a.

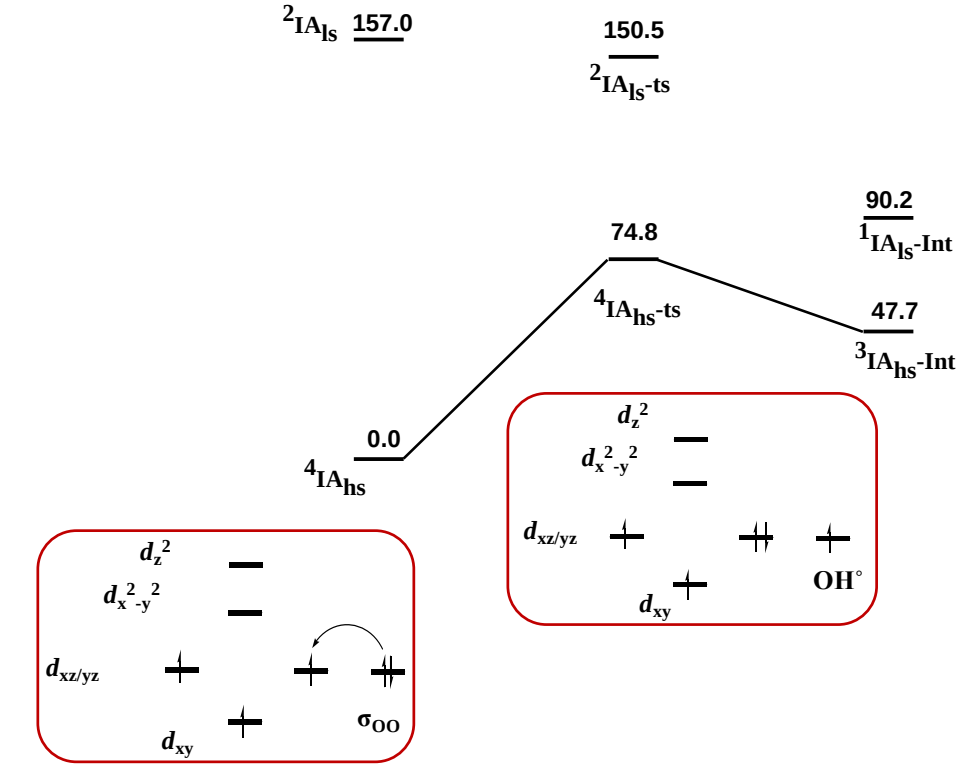

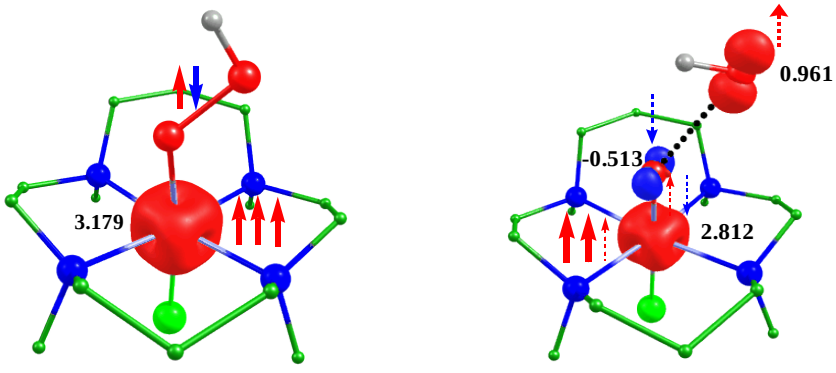

($^{4}IA_{hs}$) ($^{4}IA_{hs}$-ts)

Figure 6.1. B3LYP-D2 computed energy for the O---O bond cleavage of IA species, alongwith schematic involvement of electron and spin density plots of ground state of reactant and transition state.

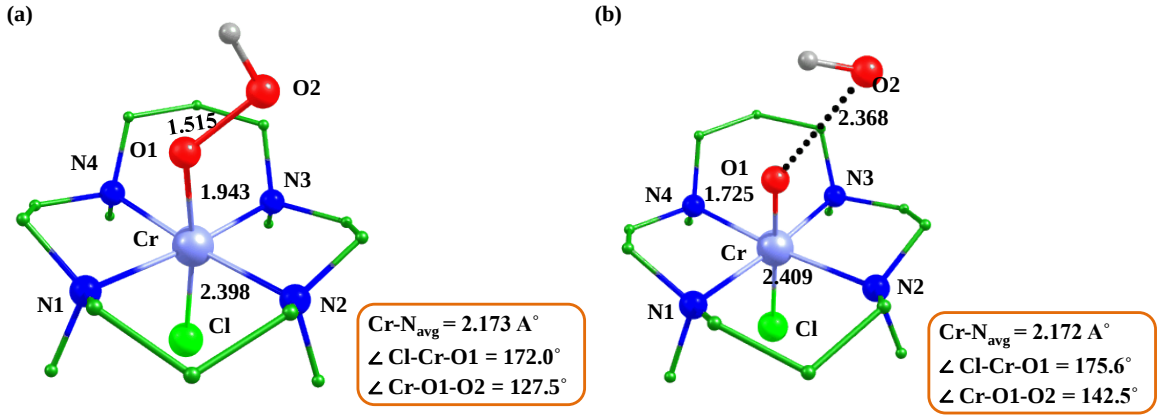

Figure 6.2. B3LYP-D2 optimized structure of ground state a) $^{4}IA_{hs}$, b) $^{4}IA_{hs}$-ts for the O---O bond cleavage of IA species.

Table 6.1. B3LYP-D2 computed selected spin density values of the 14-TMC species (reactants, transition states and products).

Spin state	Metal	O1	O2
[(14-TMC)(Cl)CrOOH, IA]$^{+}$ Species			
$^{4}IA_{hs}$	3.179	-0.001	0.040
$^{2}IA_{ls}$	1.126	-0.045	0.007
$^{4}IA_{hs}$-ts	2.812	-0.513	0.961
$^{2}IA_{ls}$-ts	0.697	-0.281	0.663
$^{3}IA_{hs}$-Int	2.784	-0.569	-
$^{1}IA_{ls}$-Int	0	0	-
[(14-TMC)(Cl)MnOOH]$^{+}$ Species			
$^{5}IIA_{hs}$	3.987	-0.010	0.042
$^{3}IIA_{is}$	2.098	0.042	0.023
$^{1}IIA_{ls}$	0.000	0.000	0.000
$^{5}IIA_{hs}$-ts	3.341	0.269	0.668
$^{3}IIA_{is}$-ts	2.493	0.272	-0.549
$^{4}IIA_{hs}$-Int	2.677	0.545	-
$^{2}IIA_{ls}$-Int	1.165	-0.061	-
[(14-TMC)(Cl)FeOOH]$^{+}$ Species			
$^{6}IIIA_{hs}$	3.980	0.277	0.051
$^{4}IIIA_{is}$	2.896	0.194	0.030

^{2}IIIA$_{ls}$	1.039	0.089	-0.000
^{6}IIIA$_{hs}$-ts	3.275	0.528	0.869
^{4}IIIA$_{is}$-ts	2.352	-0.151	0.0058
^{2}IIIA$_{ls}$-ts	1.309	0.575	-0.775
^{5}IIIA$_{hs}$-Int	3.081	0.632	-
^{3}IIIA$_{is}$-Int	1.313	0.793	-
^{1}IIIA$_{ls}$-Int	0	0	-
[(14-TMC)(Cl)CoOOH]$^{+}$ Species			
^{5}IVA$_{hs}$	2.776	0.437	0.083
^{3}IVA$_{is}$	1.829	0.173	0.013
^{1}IVA$_{ls}$	0.000	0.000	0.000
^{5}IVA$_{hs}$-ts	2.164	0.673	0.798
^{6}IVA$_{hs}$-Int	2.750	1.400	-
^{4}IVA$_{is}$-Int	1.855	0.884	-
^{2}IVA$_{ls}$-Int	-0.026	0.974	-
[(14-TMC)(Cl)NiOOH]$^{+}$ Species			
^{2}VA$_{ls}$	1.277	-0.099	-0.344
^{4}VA$_{hs}$-ts	0.936	0.928	0.853
^{5}VA$_{hs}$-Int	1.545	1.571	-
^{3}VA$_{is}$-Int	0.957	-1.156	-
[(14-TMC)(Cl)CuOOH]$^{+}$ Species			
^{3}VIA$_{hs}$	0.519	0.474	0.123
^{1}VIA$_{hs}$	0.000	0.000	0.000
^{3}VIA$_{hs}$-ts	0.030	1.231	0.796
^{4}VIA$_{hs}$-Int	0.534	1.362	-
^{2}VIA$_{ls}$-Int	-0.165	1.425	-

Computed eigenvalue plot of the ground state is shown in Figure 6.3. The electronic configuration at the metal is found to be $(d_{xy})^1$ $(d_{xz})^1$ $(d_{yz})^1$ $(d_{x^2-y^2})^0$ $(d_{z^2})^0$. Barrier height of O---O bond cleavage of species IA is computed to be 74.8 kJ/mol at high spin state (S=3/2; ^{4}IA$_{hs}$-ts), and 150.5 kJ/mol for low spin state (S=1/2; ^{2}IA$_{ls}$-ts; see Figure 6.1). The optimized structure and spin density plot of the ^{4}IA$_{hs}$ and ^{4}IA$_{hs}$-ts are shown in Figure 6.2. The computed Cr-O and Cr-N$_{avg}$ bond length decreases 1.943/1.725 Å, 2.173/2.172 Å, respectively, while O1-O2 and Cr-Cl bond length increases 1.515/2.368 Å, 2.398/2.409 Å

respectively, and these parameters confirm the transition state of O---O bond cleavage. Computed spin density during the O---O bond cleavage at chromium center ($^4IA_{hs}$-ts) decreases 3.179/2.812 and spin density at O1 and O2 is computed to be -0.513 and 0.961, respectively, (see Figure 6.1) indicates that O---O bond cleaves as homolytically fashion. During O---O bond cleavage, beta (β) electron (see Figure 6.1) is shifted from $^4IA_{hs}$ to $d_{xz/yz}$ of $^4IA_{hs}$-ts to form the π bond which is also supported by the bond angle of 142.5^0 (see Table AX 6.1 of appendix).[62] Bond Parameters and decreasing spin density at chromium center shows the formation of π-bond between the up spin of chromium and the down spin at O1 (see Table 6.1). Spin natural orbital (SNO) analysis shows the transfer of an electron to the metal *d* orbital (see Figure 6.4). This O---O bond cleavage is also supported by computed wiberg bond indices (see Table AX 6.2 of appendix). More, electron-electron (*d*-*d*) exchange interaction decreases electron-electron repulsion and stabilizes the transition state and this may be a reason for the lower barrier at a high spin state (see Figure 6.1).

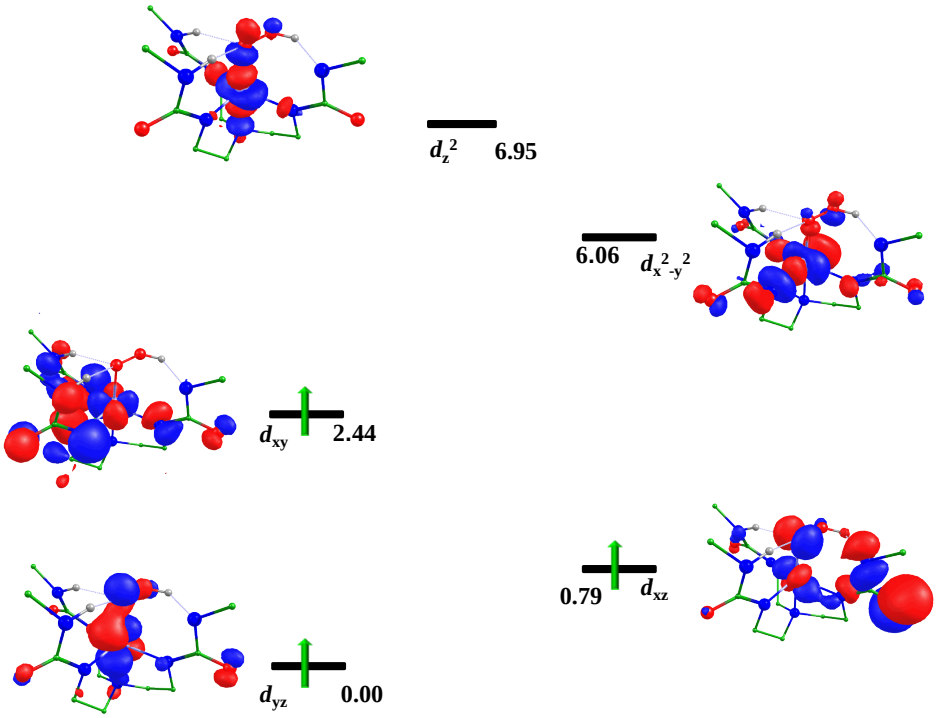

Figure 6.3 Computed eigenvalue plot incorporating energies computed for *d*-based orbitals for alpha corresponding to the ground state $^4IA_{hs}$ of the complex IA (energies are given in eV).

(a)

($^4IA_{hs}$)

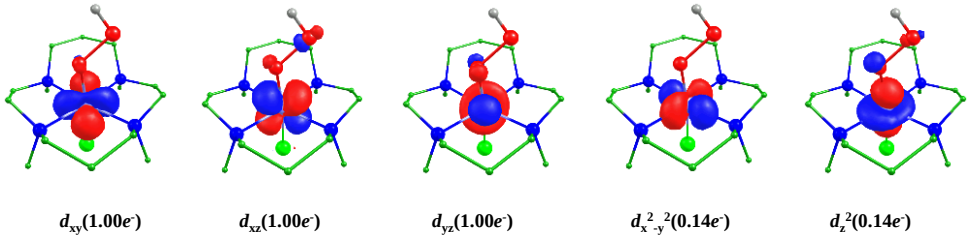

$d_{xy}(1.00e^-)$ $d_{xz}(1.00e^-)$ $d_{yz}(1.00e^-)$ $d_{x^2-y^2}(0.14e^-)$ $d_{z^2}(0.14e^-)$

($^4IA_{hs}$-ts)

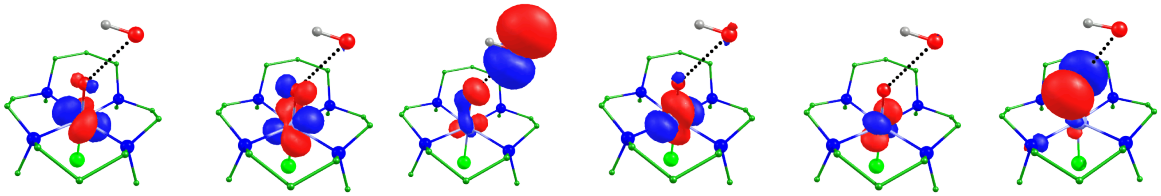

$d_{xy}(1.00e^-)$ $d_{xz}(1.00e^-)$ $d_{yz}(1.00e^-)$ $d_{x^2-y^2}(0.14e^-)$ $d_{z^2}(0.64e^-)$ $d_{yz}(-0.64e^-)$

(b)

$^5IIA_{hs}$

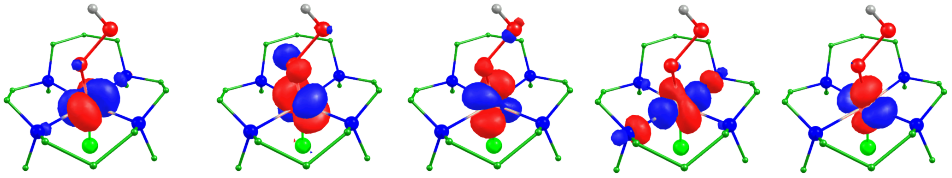

$d_{xy}(1.00e^-)$ $d_{xz}(1.00e^-)$ $d_{yz}(1.00e^-)$ $d_{x^2-y^2}(1.00e^-)$ $d_{z^2}(0.30e^-)$

$^5IIA_{hs}$-ts

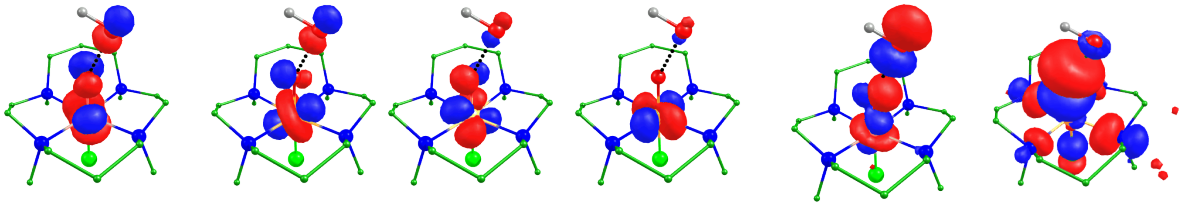

$d_{xy}(1.00e^-)$ $d_{xz}(1.00e^-)$ $d_{yz}(1.00e^-)$ $d_{x^2-y^2}(0.27e^-)$ $d_{z^2}(1.00e^-)$ $d_{xz}(-0.26e^-)$

(c)

$^6IIIA_{hs}$-ts

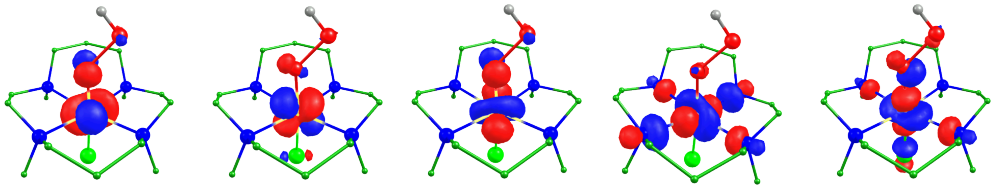

$d_{xy}(1.00e^-)$ $d_{xz}(1.00e^-)$ $d_{yz}(1.00e^-)$ $d_{x^2-y^2}(1.00e^-)$ $d_{z^2}(1.00e^-)$

$^6IIIA_{hs}$-ts

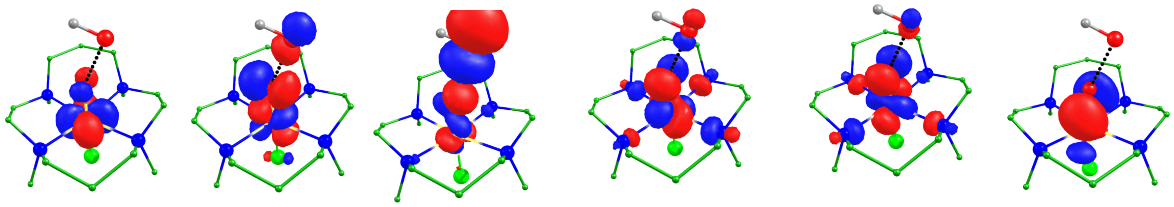

$d_{xy}(1.00e^-)$ $d_{xz}(1.00e^-)$ $d_{yz}(1.00e^-)$ $d_{x^2-y^2}(1.00e^-)$ $d_{z^2}(1.00e^-)$ $d_{xz}(-0.07e^-)$

Figure 6.4. Spin natural orbitals and their occupations (noted in parenthesis) of a) $^{4}IA_{hs}$, $^{4}IA_{hs}$-ts, b) $^{5}IIA_{hs}$, $^{5}IIA_{hs}$-ts, and c) $^{6}IIIA_{hs}$, and $^{6}IIIA_{hs}$-ts.

On moving right in the periodic table from chromium to manganese and iron, one and two extra electrons are added to *d* orbitals, respectively. Similar to chromium species, we have performed the same calculations on manganese and iron species and computed that high spin state (S=2, $^{5}IIA_{hs}$, and S=5/2, $^{6}IIIA_{hs}$) are the ground state in Mn, and Fe species, respectively. The computed spin energetic of other spin states is shown in Figure 6.5 and Figure 6.6.

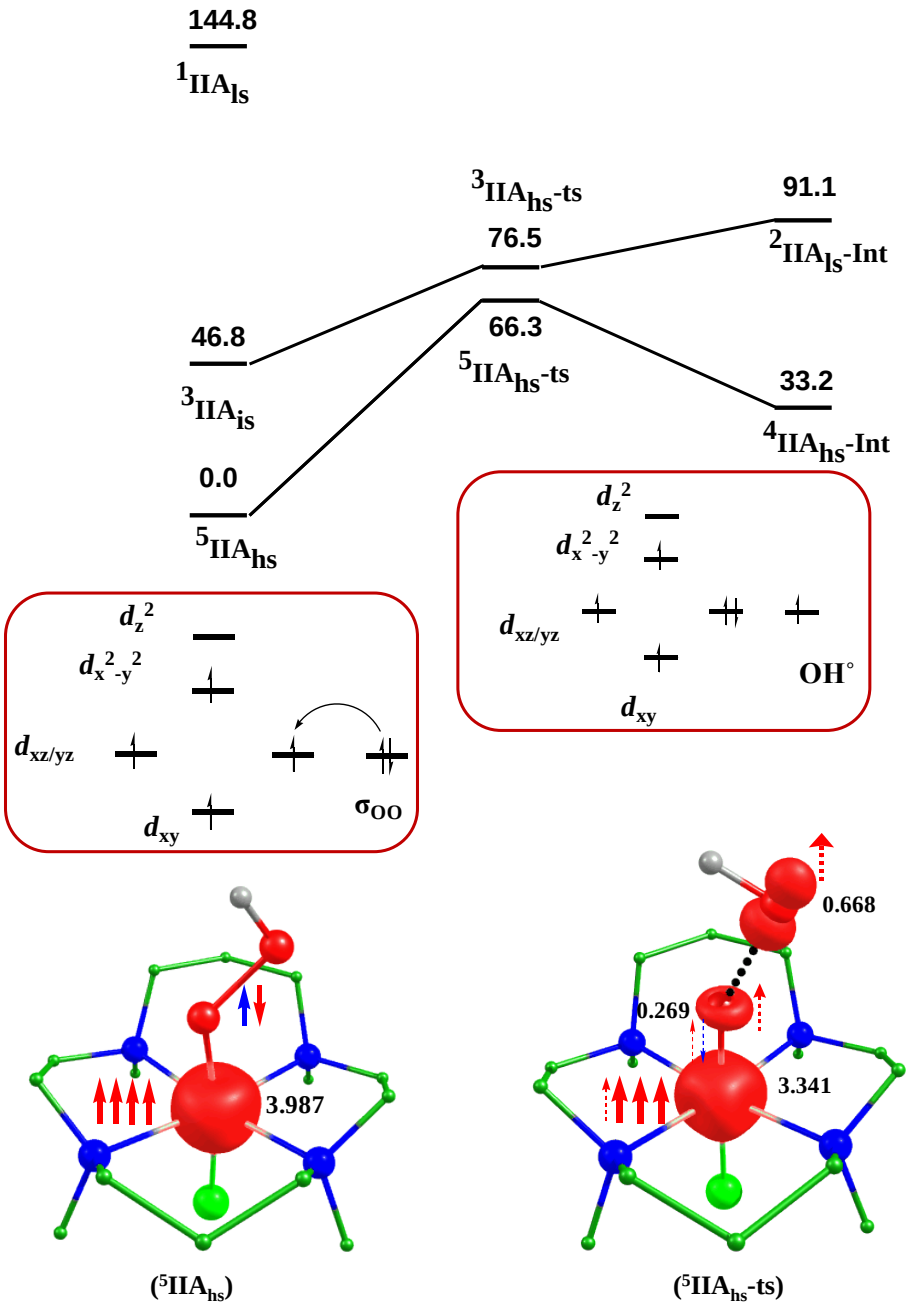

Figure 6.5 B3LYP-D2 computed energy for the O---O bond cleavage of IIA species. The computed barrier height is shown with respect to the reactant (IIA).

The optimized structures of ground state of IIA and IIIA are shown in Figure 6.7a,c. The electronic configuration at the manganese is found to be $(d_{xy})^1$ $(d_{xz})^1$ $(d_{yz})^1$ $(d_{x^2-y^2})^1$ $(d_{z^2})^0$ and at iron center it is found to be $(d_{xy})^1$ $(d_{xz})^1$ $(d_{yz})^1$ $(d_{x^2-y^2})^1$ $(d_{z^2})^1$ (see Figure 6.8). During O---O bond cleavage computed bond parameter shows that Mn-O, Mn-N_{avg}, and Fe-O, Fe-N_{avg} bond length decreased 1.916/1.748 Å, 2.236/2.156 Å, and 1.953/1.677 Å, 2.249/2.221 Å respectively, and O-O, Mn/Fe-Cl bond length increases 1.511/1.854 Å, 2.344/2.433 Å, and 1.495/2.052 Å, 2.378/2.322 Å with Mn and iron species respectively.

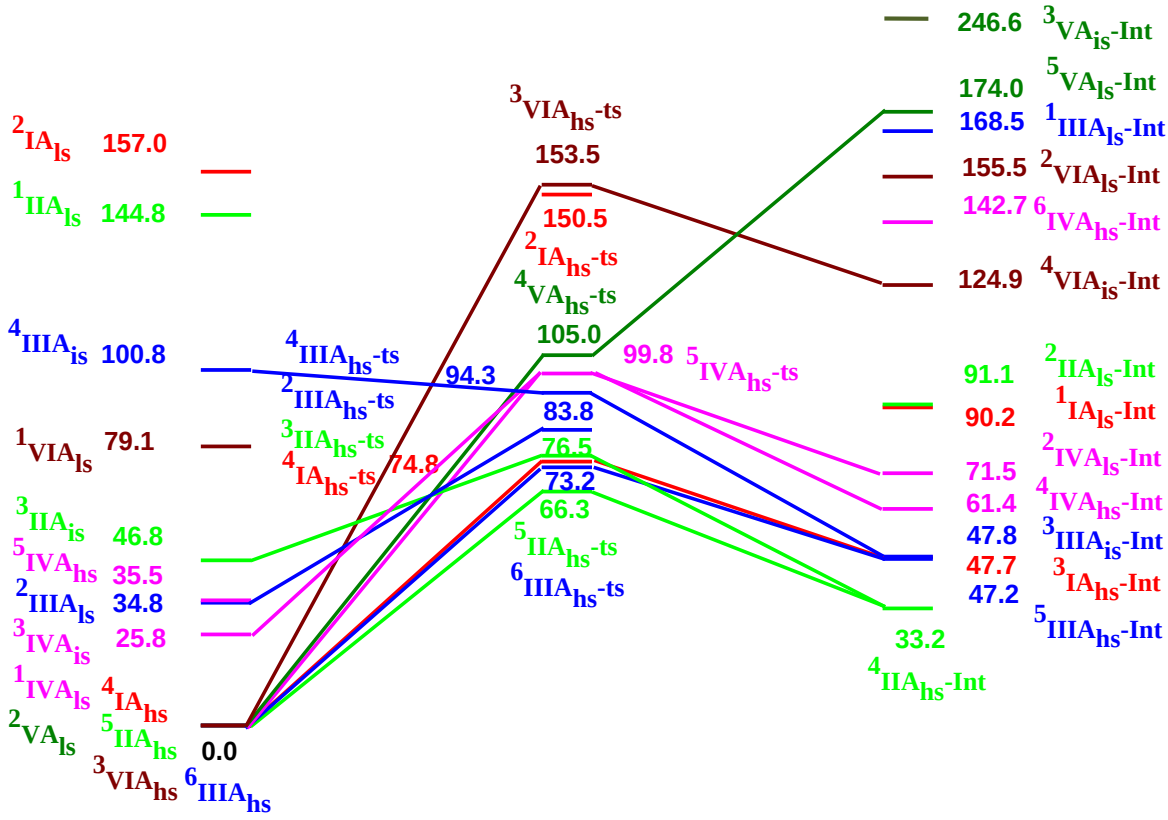

Figure 6.6. B3LYP-D2 computed energy surface for the formation of metal-oxo from metalhydroperoxo with buea ligand chromium (red), manganese (green), iron (blue), cobalt (magneta), nickel (olive), and copper (wine).

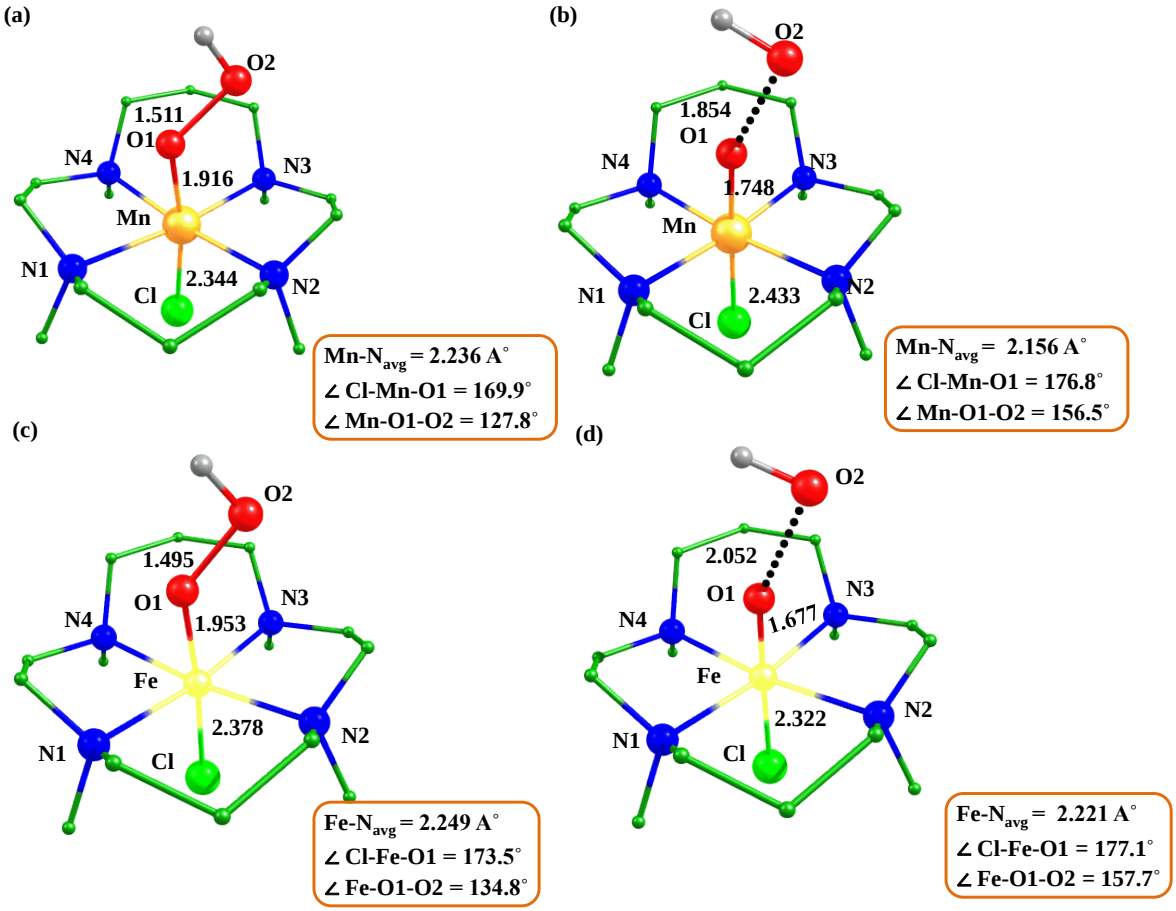

Figure 6.7. B3LYP-D2 a,b) optimized structure (bond length in Å) of ^{5}IIA$_{hs}$, ^{5}IIA$_{hs}$-ts, ^{6}IIIA$_{hs}$and ^{6}IIIA$_{hs}$-ts.

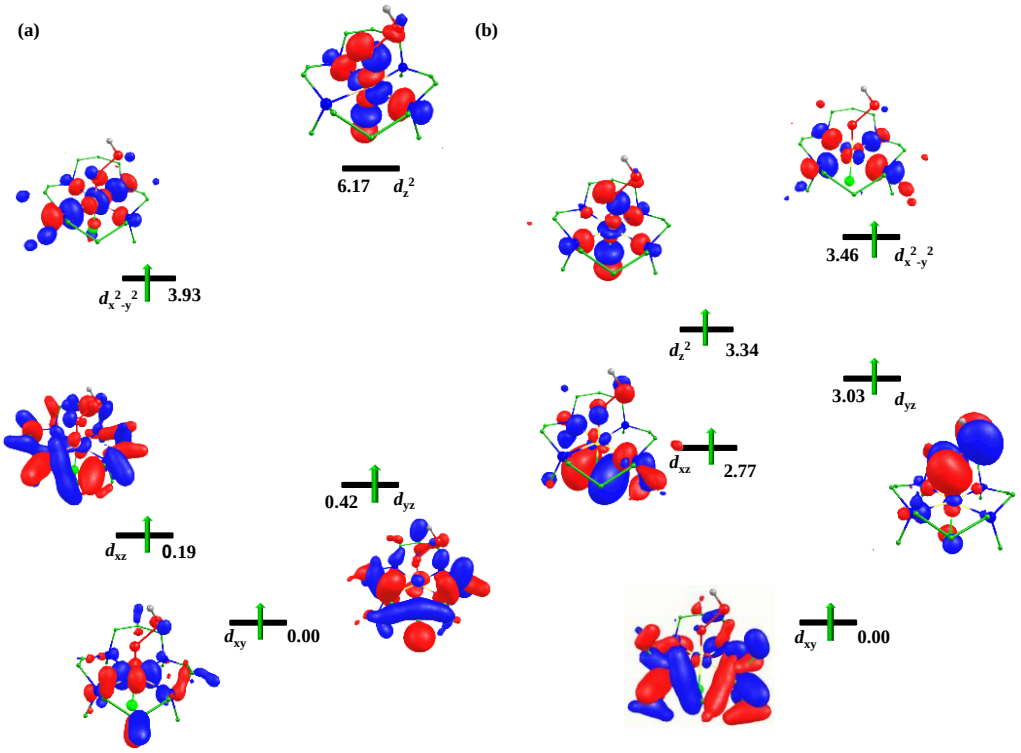

Figure 6.8. Computed eigenvalue plot incorporating energies computed for *d*-based orbitals for alpha corresponding to the ground state $^{5}IIA_{hs}$ of the species IIA, b) $^{6}IIIA_{hs}$ of the species IIIA (energies are given in eV).

Computed spin density at Mn and Fe center decreases 3.987/3.341, 3.980/3.275 respectively, and spin density at O1 and O2 during O---O bond cleavage are found to be 0.269/0.668 and 0.528/0.869 with Mn, Fe species, respectively, these spin density shows that the O---O bond cleavage occurs via homolytic manner. The barrier height of O---O bond cleavage is computed to be 63.3 kJ/mol with manganese and 73.2 kJ/mol with iron (see PES Figure 6.5 and Figure 6.6). Spin natural orbital of ground state of IIA and IIIA species and their transition state during O---O bond cleavage are shown in Figure 6.4, which shows the transfer of electron during O---O bond cleavage.

On moving right in 3*d* series, pairing of electrons starts in cobalt (IVA), nickel (VA), and copper (VIA) species.[25] Computed energetics suggests that $^{5}IVA_{hs}$, $^{2}VA_{ls}$, and $^{3}VIA_{hs}$ spin states are ground states (see Figure 6.6). Computed barrier height of O---O bond cleavage at ground state are 99.8 kJ/mol ($^{5}IVA_{hs}$-ts), 105.1 kJ/mol ($^{4}VA_{hs}$-ts), and 153.5 kJ/mol ($^{3}VIA_{hs}$-ts) with cobalt, nickel and copper species (see Figure 6.6). The optimized structure of ground states of $^{5}IVA_{hs}$, $^{2}VA_{ls}$, and $^{3}VIA_{hs}$ species and their corresponding transition states are shown in Figure 6.9.

M-O1 bond length in metal hydroperoxo species to the transition state decreases 1.934/1.674 Å, 2.013/1.836 Å, 2.291/2.004 Å, with cobalt, nickel and copper species respectively. Electron density at metal center decreases 2.766/2.164, 1.588/0.936, 0.519/0.030, with Co, Ni, and Cu species respectively. Computed significant electron density at oxygen atoms O1 and O2 are 0.673/0.798, 0.928/0.853, and 1.231/0.796, at Co, Ni and Cu species, respectively, confirm the homolytic O---O bond cleavage. The angle during the transition state of the M-O---O bond cleavage are computed to be 156.5˚ ($^{5}IIA_{hs}$-ts), 157.7˚ ($^{6}IIIA_{hs}$-ts),

162.5° (^{5}IVA$_{hs}$-ts), 154.1° (^{4}VA$_{hs}$-ts), and 135.5° (^{3}VIA$_{hs}$-ts) (see Table AX 6.1 of appendix) shows O---O bond cleavage takes place via π-pathway rather than σ-pathway. The barrier heights of O---O bond cleavage in the manganese and iron species is lower at high spin state (^{5}IIA$_{hs}$-ts) and (^{6}IIIA$_{hs}$-ts) than corresponding to their other spin states (^{3}IIA$_{hs}$-ts, ^{4}IIIA$_{hs}$-ts, and ^{2}IIIA$_{hs}$-ts) because of enhanced exchanged reactivity (see Figure 6.5 and Figure 6.6) and higher barrier height in late transition series because pairing of electron strats in late transition series (see Figure 6.10).

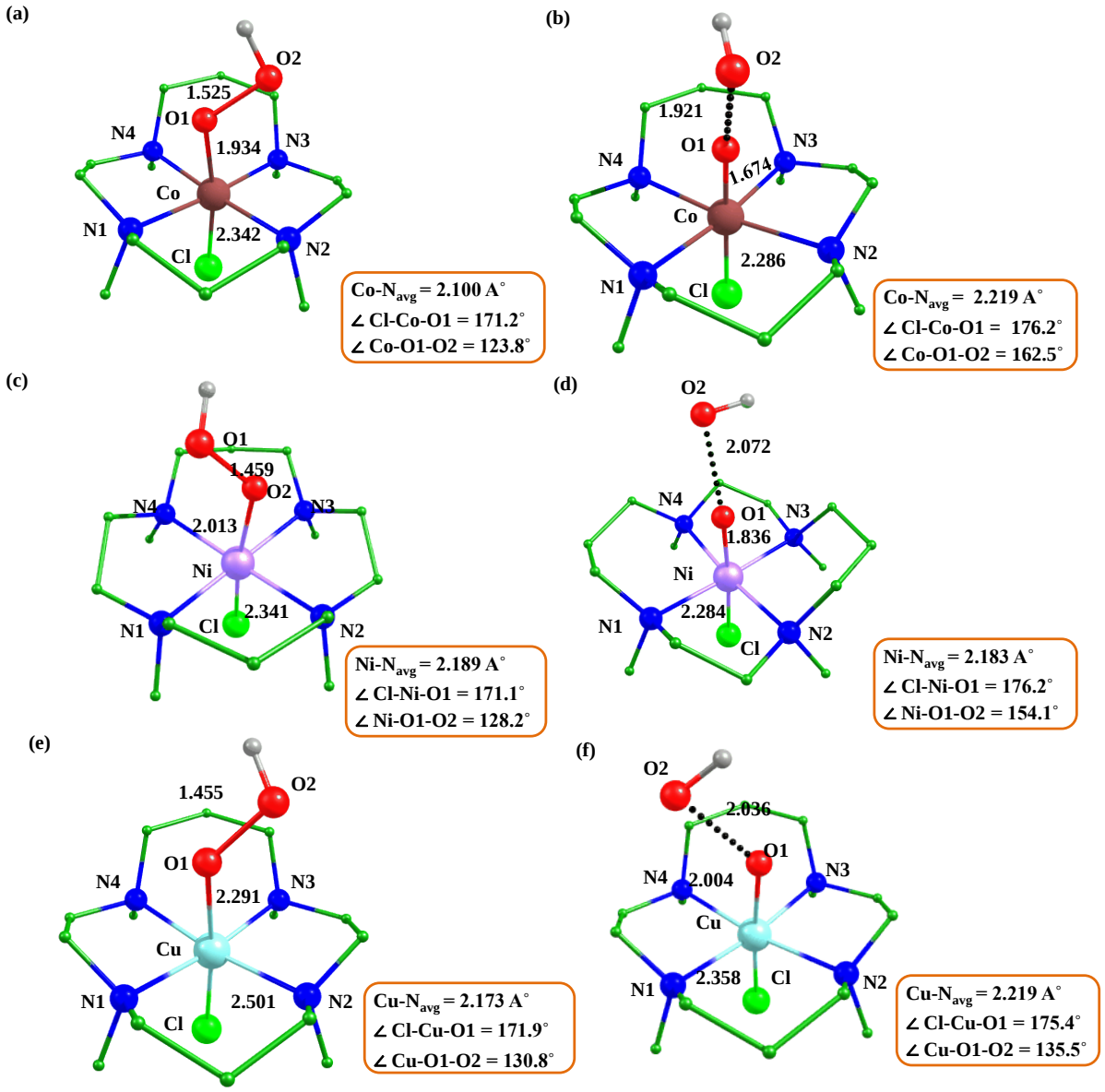

Figure 6.9. B3LYP-D2 optimized structure a) cobalt (^{1}IVA$_{ls}$), b) its transition state ^{5}IVA$_{hs}$-ts), (^{4}VA$_{hs}$-ts), c) optimized structure of nickel (^{2}VA$_{ls}$), d) its corresponding transition state (^{4}VA$_{hs}$-ts), e) optimized structure of ^{3}VIA$_{hs}$ and f) its corresponding transition state(^{3}VIA$_{hs}$-ts).

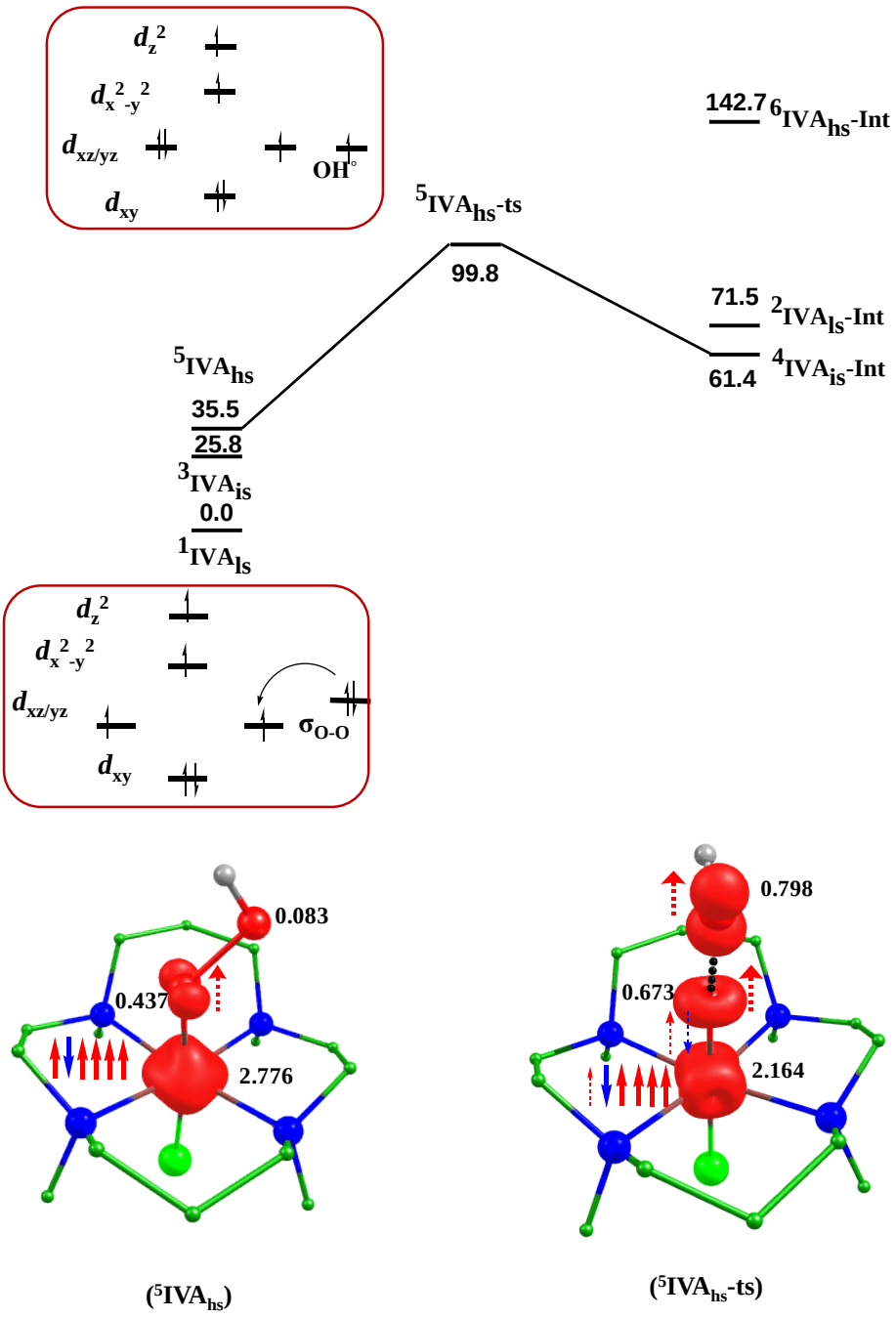

Figure 6.10. B3LYP-D2 computed energy for the O-O bond cleavage of IVA species. The computed barrier height is shown with respect to the reactant (IVA).

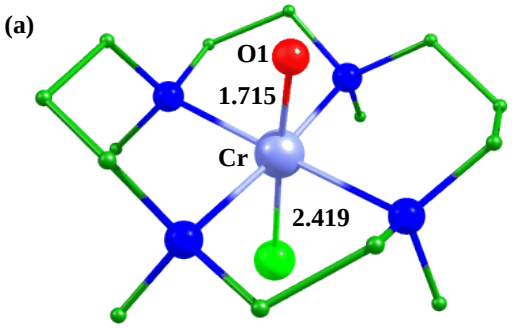

Cr-N_{avg} = 2.171 A°

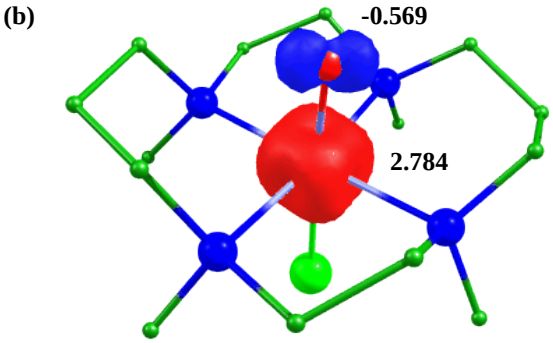

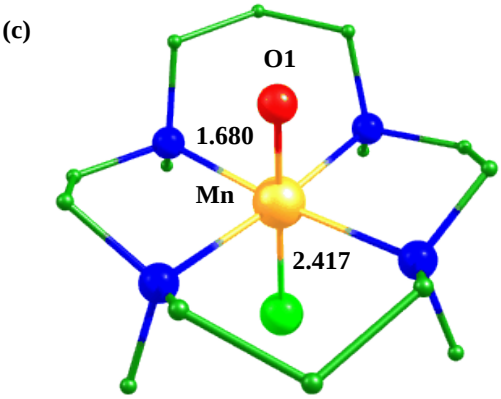

Mn-N_{avg} = 2.145 A°

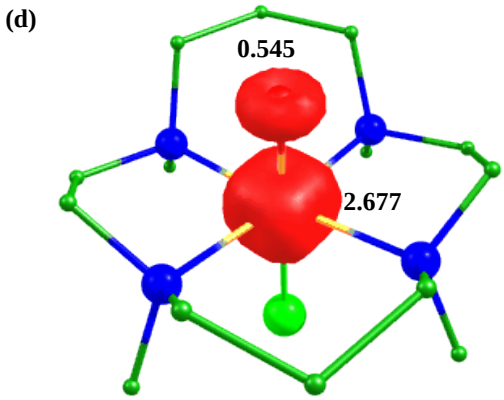

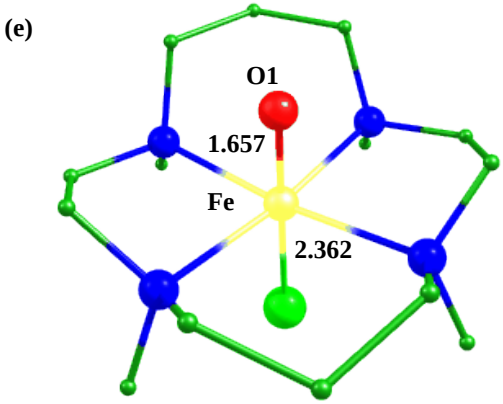

Fe-N_{avg} = 2.219 A°

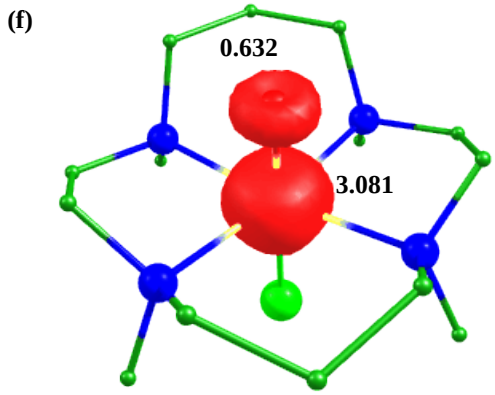

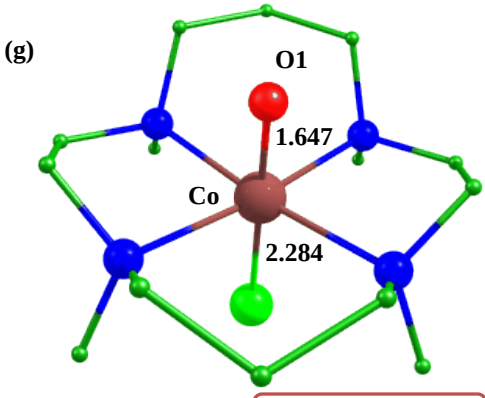

Co-N_{avg} = 2.210 A°

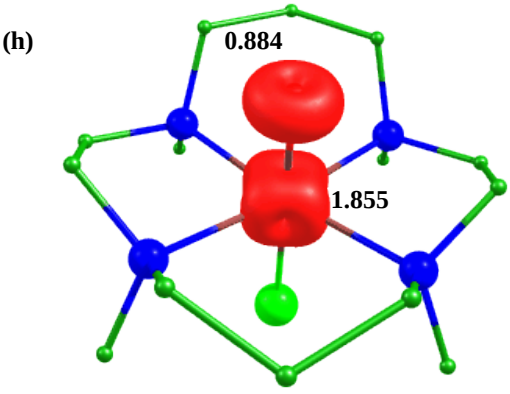

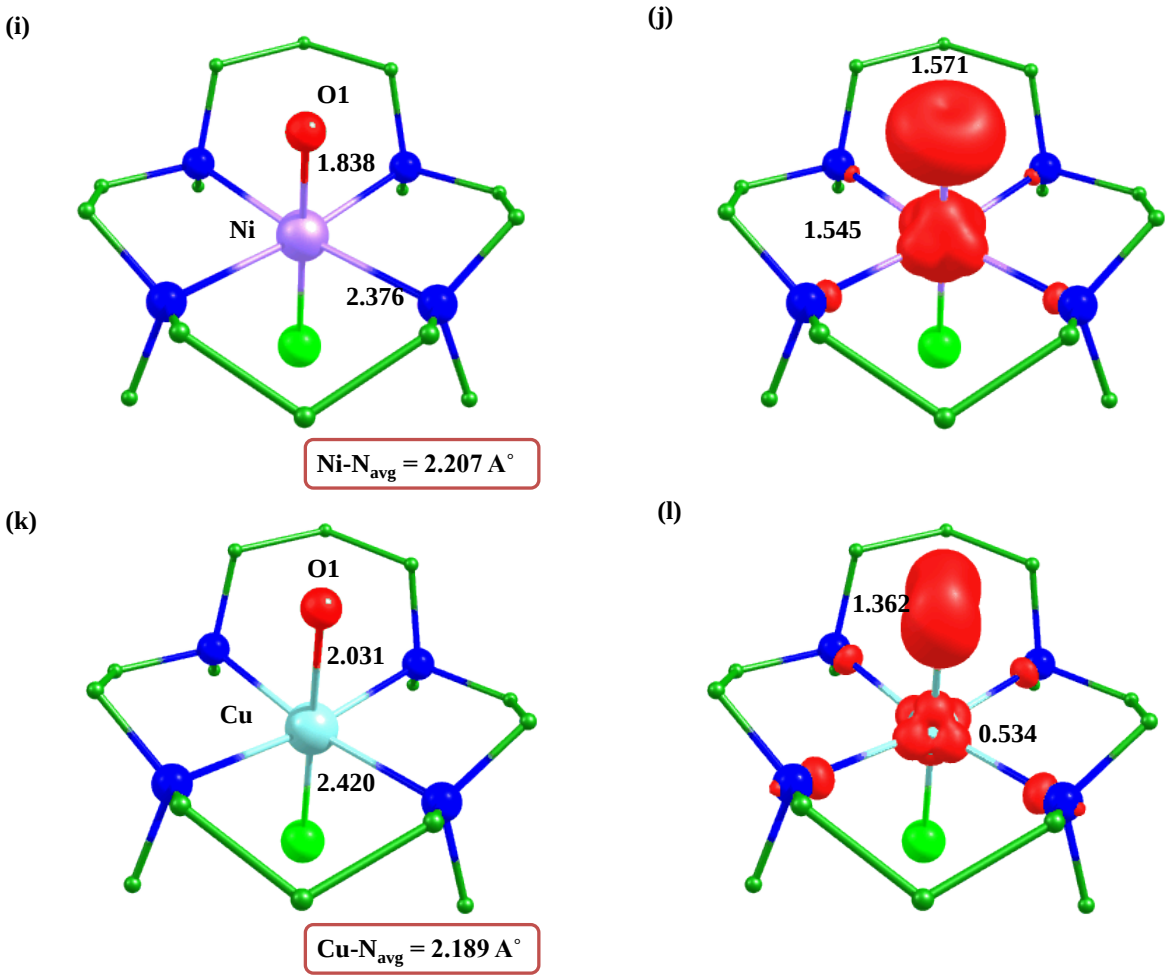

Figure 6.11. B3LYP-D2 a) optimized structure (bond length in Å) b) spin density plot of $^{3}IA_{hs}$-Int; c) optimized structure (bond length in Å) d) spin density plot of $^{4}IIA_{hs}$-Int; e) optimized structure (bond length in Å) f) spin density plot of $^{5}IIIA_{hs}$-Int and $^{5}IIIA_{hs}$-ts; g) optimized structure (bond length in Å) h) spin density plot of $^{4}IVA_{is}$-Int; i) optimized structure (bond length in Å); j) spin density plot of $^{5}VA_{hs}$-Int; k) optimized structure (bond length in Å) and l) spin density plot of $^{4}VIA_{hs}$-Int.

The O---O bond cleavage leads to the formation of metal-oxo species. We have computed all the possible spin states of metal-oxo species. On the basis of their energetics $^{3}IA_{hs}$-Int, $^{4}IIA_{hs}$-Int, $^{5}IIIA_{hs}$-Int, $^{4}IVA_{is}$-Int, $^{5}VA_{hs}$-Int and $^{4}VIA_{hs}$-Int spin states are found to be ground state with IA, IIA, IIIA, IVA, VA and VIA species. Optimized structures and corresponding spin density plots of the ground state of metal-oxo species are shown in Figure 6.11. Selected bond parameters of the studied metal-oxo species are shown in Table AX 6.1 of appendix.

Significant electron density at the oxygen atom may be a witness for the reactive nature of metal-oxo species. We have also computed the M-O stretching frequencies (see Table 6.2).

Table 6.2. Computed stretching frequencies of M-O bond in metal-oxo species.

Metal-oxo	υ (cm^{-1})	Spin State	υ (cm^{-1})
$^{3}IA_{hs}$-Int	558	$^{3}IB_{hs}$-Int	921
$^{4}IIA_{hs}$-Int	869	$^{4}IIB_{hs}$-Int	851
$^{5}IIIA_{hs}$-Int	872	$^{5}IIIB_{hs}$-Int	889
$^{4}IVA_{is}$-Int	849	$^{4}IVB_{is}$-Int	515
$^{5}VA_{hs}$-Int	499	$^{5}VB_{hs}$-Int	390
$^{4}VIA_{hs}$-Int	376	$^{4}VIB_{hs}$-Int	419

6.3.2 Metal hydroperoxo species with buea ligand (IB (chromium), IIB (manganese), IIIB (iron), IVB (cobalt), VB (nickel) and VIB (copper))

We have also enlightened theoretical study from octahedral geometry to trigonal bipyramidal (cavity). So, similar to TMC species, first we have performed optimization on all possible spin surfaces of (buea) Cr-OOH to (buea) Cu-OOH species and also their transition states of O---O bond cleavage. On the basis of energetic it is found that $^{4}IB_{hs}$, $^{5}IIB_{hs,}$ $^{6}IIIB_{hs,}$ $^{4}IVB_{is,}$ $^{4}VB_{hs}$ and $^{4}VIB_{hs}$ spin states are the ground state. Spin energetic at other spin states are also shown in Figure 6.12. Selected bond parameters are shown in Table AX 6.3 of appendix. Selected spin density are shown in Table 6.3. Optimized structures and spin density plots of ground state of metal hydroperoxo IB, IIB, IIIB, IVB, VB and VIB species are shown in Figure 6.13a,c,e,g,i,k. Our DFT calculations show that the computed barrier height of ground state O---O cleavage are 90.2 kJ/mol ($^{2}IB_{hs}$-ts; Cr), 83.6 kJ/mol ($^{5}IIB_{hs}$-ts; Mn), 57.7 kJ/mol

(^{4}IIIB$_{hs}$-ts; Fe), 119.2 kJ/mol (^{5}IVB$_{hs}$-ts; Co), 99.8 kJ/mol (^{4}VB$_{hs}$-ts; Ni) and 154.0 kJ/mol (^{1}VIB$_{hs}$-ts; Cu species) and spin energetics of other spin surfaces (see Figure 6.12).

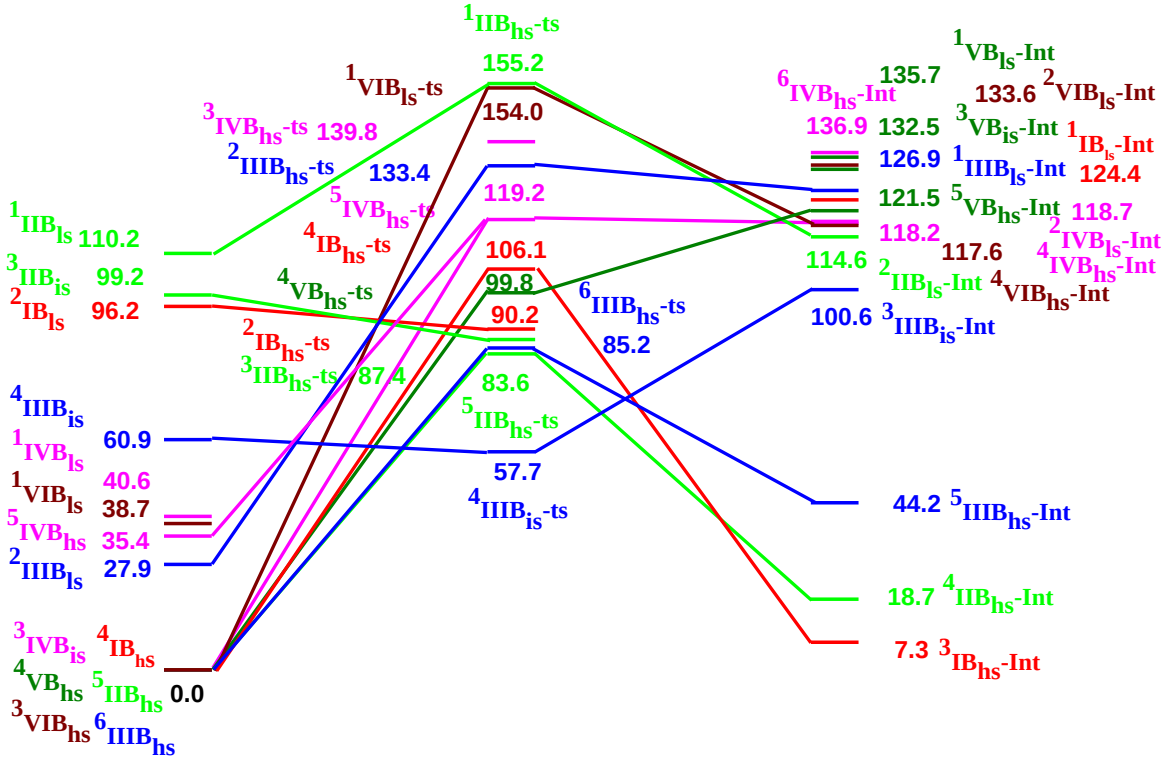

Figure 6.12. B3LYP-D2 computed energy surface for the formation of metal-oxo from metalhydroperoxo with buea ligand Chromium (red), manganese (green), iron (blue), cobalt (magenta), nickel (olive), and copper (wine).

Table 6.3. B3LYP-D2 computed spin density values of the buea species (reactant, transition states, and product).

Spin State	Metal	O_1	O_2
[(buea)CrOOH]$^{-}$			
^{4}IB$_{hs}$	3.005	-0.009	0.012
^{2}IB$_{ls}$	0.991	0.040	-0.009
^{4}IB$_{hs}$-ts	2.549	-0.024	0.545
^{2}IB$_{ls}$-ts	1.089	0.043	-0.111
^{3}IB$_{hs}$-Int	1.930	0.050	-
^{1}IB$_{ls}$-Int	0	0	-
[(buea)MnOOH]$^{-}$			
^{5}IIB$_{hs}$	3.831	-0.038	0.007
^{3}IIB$_{is}$	1.929	0.025	-0.012
^{1}IIB$_{ls}$	0.000	0.00	0.000

$^{5}IIB_{hs}$-ts	3.301	0.056	0.577
$^{3}IIB_{is}$-ts	2.238	0.094	-0.312
$^{1}IIB_{ls}$-ts	0.000	0.000	0.000
$^{4}IIB_{hs}$-Int	2.732	0.256	-
$^{2}IIB_{ls}$-Int	1.004	-0.112	-
[(buea)FeOOH]$^{-}$			
$^{6}IIIB_{hs}$	3.926	0.228	0.026
$^{4}IIIB_{is}$	2.771	-0.017	-0.031
$^{2}IIIB_{ls}$	0.979	0.002	-0.005
$^{6}IIIB_{hs}$-ts	3.381	0.258	0.742
$^{4}IIIB_{is}$-ts	2.826	0.291	-0.631
$^{2}IIIB_{ls}$-ts	1.399	0.080	-0.481
$^{5}IIIB_{hs}$-Int	2.991	0.456	-
$^{3}IIIB_{is}$-Int	1.569	0.375	-
$^{1}IIIB_{ls}$-Int	0	0	-
[(buea)CoOOH]$^{-}$			
$^{5}IVB_{hs}$	2.744	0.206	0.017
$^{3}IVB_{is}$	1.719	-0.117	-0.034
$^{1}IVB_{ls}$	0.000	0.000	0.000
$^{5}IVB_{hs}$-ts	2.107	0.526	0.506
$^{3}IVB_{is}$-ts	1.423	0.279	0.553
$^{6}IVB_{hs}$-Int	2.701	1.044	-
$^{4}IVB_{is}$-Int	1.701	0.664	-
$^{2}IVB_{ls}$-Int	1.562	-0.956	-
[(buea)NiOOH]$^{-}$			
$^{4}VB_{hs}$	1.640	0.229	0.023
$^{2}VB_{ls}$	0.927	-0.135	-0.052
$^{2}VB_{ls}$-ts	0.929	0.336	0.456
$^{5}VB_{hs}$-Int	1.615	1.104	-
$^{3}VB_{is}$-Int	1.634	-0.808	-
$^{1}VB_{ls}$-Int	0	0	-
[(buea)CuOOH]$^{-}$			
$^{3}VIB_{hs}$	0.494	0.344	0.086
$^{1}VIB_{ls}$	0.000	0.000	0.000
$^{1}VIB_{ls}$-ts	0	0	0
$^{4}VIB_{hs}$-Int	0.524	1.169	-
$^{2}VIB_{ls}$-Int	0.493	1.115	-

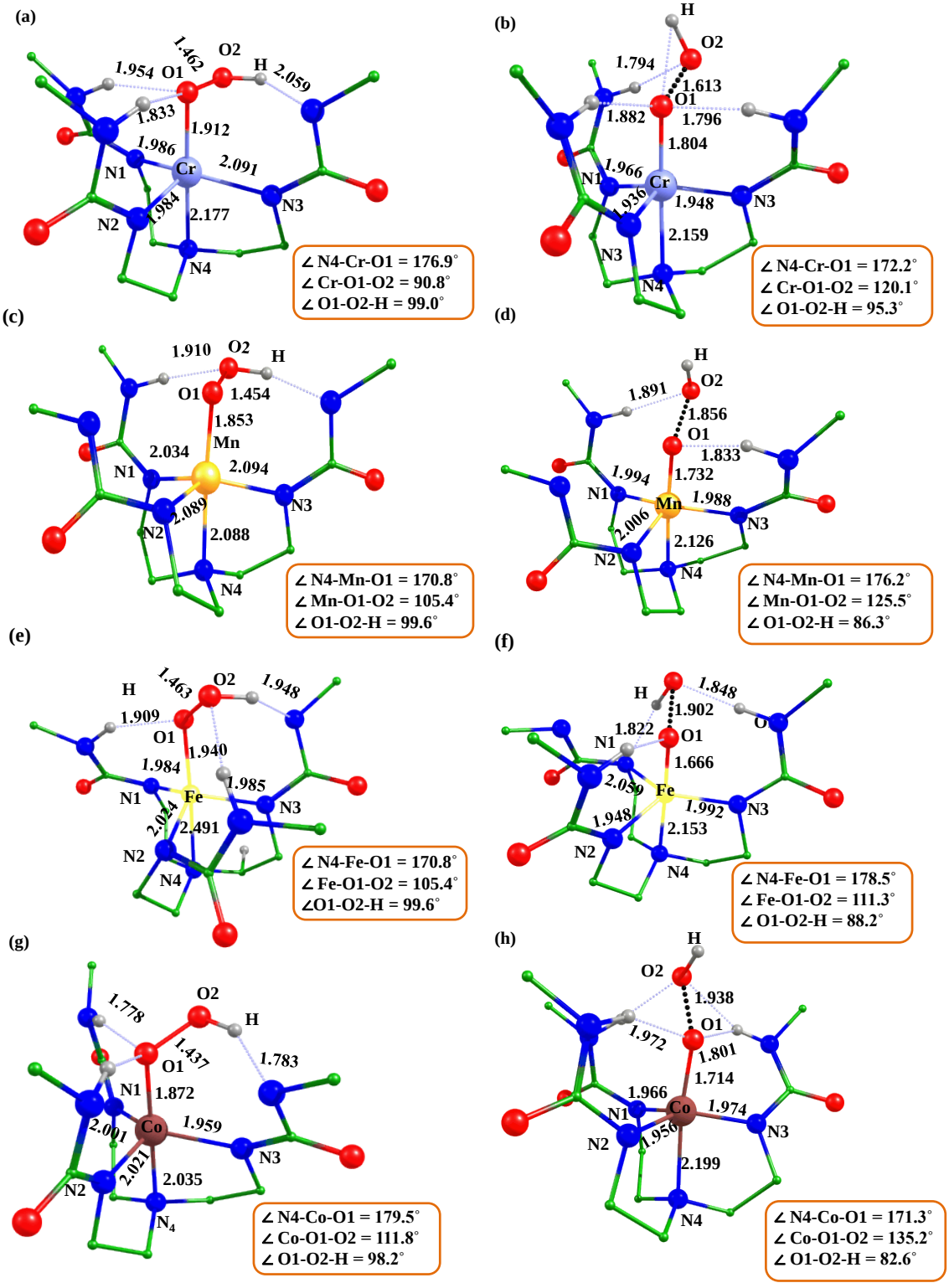
(a)
1.462
O2
H
2.059
1.954
O1
1.833
1.912
1.986
Cr
2.091
N1
N3
1.984
2.177
N2
N4
∠ N4-Cr-O1 = 176.9°
∠ Cr-O1-O2 = 90.8°
∠ O1-O2-H = 99.0°
(b)
H
O2
1.794
1.613
O1
1.882
1.796
1.804
1.966
N1
Cr
1.936
1.948
N3
2.159
N3
N4
∠ N4-Cr-O1 = 172.2°
∠ Cr-O1-O2 = 120.1°
∠ O1-O2-H = 95.3°
(c)
1.910
O2
H
O1
1.454
1.853
Mn
2.034
2.094
N1
N3
2.089
N2
2.088
N4
∠ N4-Mn-O1 = 170.8°
∠ Mn-O1-O2 = 105.4°
∠ O1-O2-H = 99.6°
(d)
H
1.891
O2
1.856
O1
1.833
1.994
1.732
N1
Mn
1.988
N3
2.006
2.126
N2
N4
∠ N4-Mn-O1 = 176.2°
∠ Mn-O1-O2 = 125.5°
∠ O1-O2-H = 86.3°
(e)
H
1.463
O2
1.948
1.909
O1
1.940
1.984
1.985
N1
Fe
N3
2.024
2.491
N2
N4
∠ N4-Fe-O1 = 170.8°
∠ Fe-O1-O2 = 105.4°
∠O1-O2-H = 99.6°
(f)
H
1.848
1.902
O
1.822
N1
O1
1.666
2.039
Fe
1.992
N3
1.948
2.153
N2
N4
∠ N4-Fe-O1 = 178.5°
∠ Fe-O1-O2 = 111.3°
∠ O1-O2-H = 88.2°
(g)
1.778
O2
H
1.437
1.783
O1
N1
1.872
2.001
Co
1.959
N3
2.021
2.035
N2
N4
∠ N4-Co-O1 = 179.5°
∠ Co-O1-O2 = 111.8°
∠ O1-O2-H = 98.2°
(h)
H
O2
1.938
O1
1.972
1.801
1.714
1.966
N1
Co
1.974
N3
1.956
N2
2.199
N4
∠ N4-Co-O1 = 171.3°
∠ Co-O1-O2 = 135.2°
∠ O1-O2-H = 82.6°

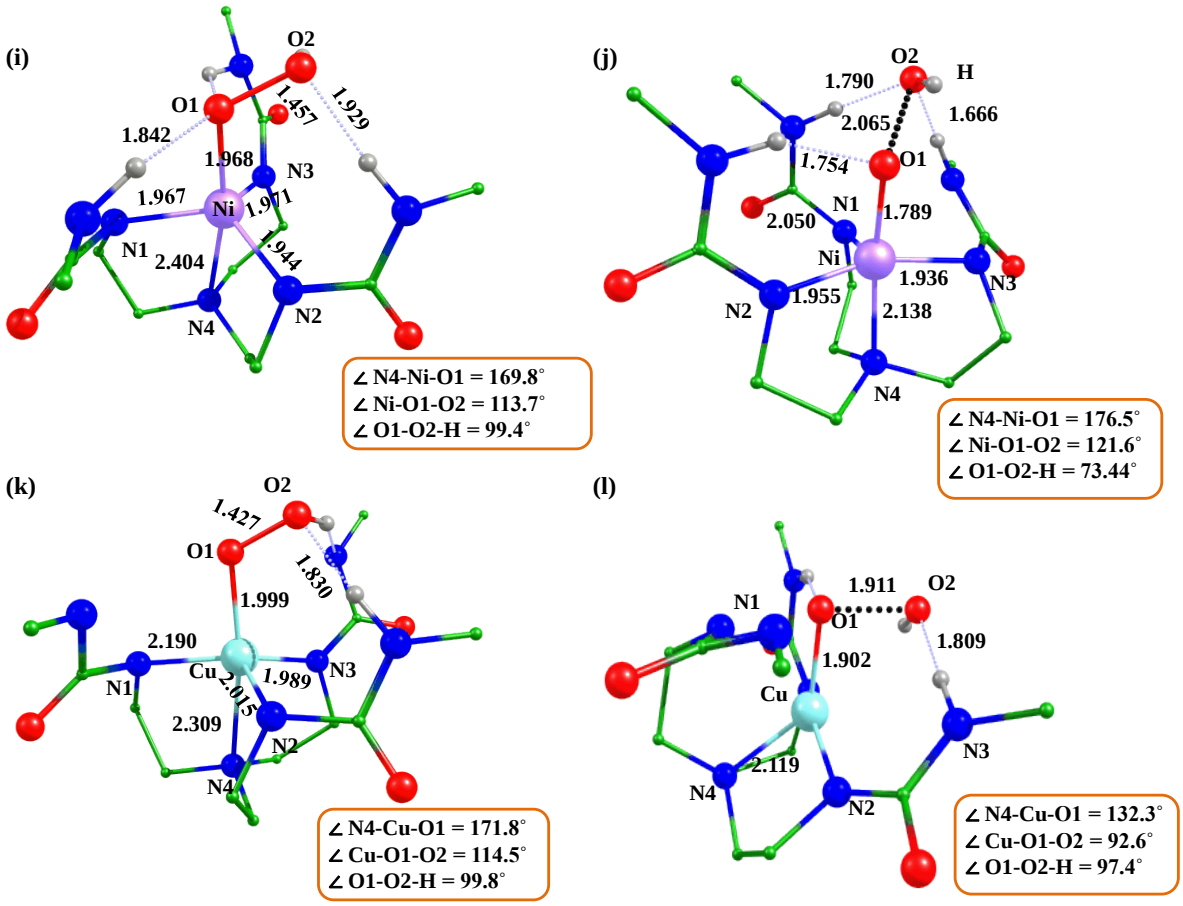

Figure 6.13. B3LYP-D2 optimized structure of ground state $^{4}IB_{hs}$, $^{5}IIB_{hs}$, $^{6}IIIB_{hs}$, $^{3}IVB_{is}$ and $^{4}VB_{hs,}$ and their corresponding transition states $^{2}IB_{ls}$-ts, $^{5}IIB_{hs}$-ts, $^{4}IIIB_{hs}$-ts, $^{5}IVB_{is}$-ts, $^{2}VB_{ls}$-ts.

Optimized structure of ground state of O---O bond cleavage $^{2}IB_{hs}$-ts, $^{5}IIB_{hs}$-ts, $^{4}IIIB_{hs}$-ts, $^{5}IVB_{hs}$-ts, $^{4}VB_{hs}$-ts, and $^{1}VIB_{hs}$-ts are shown in Figure 6.13 b,d,f,h,j,l. Computed M-O bond length decreases during O---O bond cleavage i.e. 1.912/1.804 Å (Cr), 1.853/1.732 Å (Mn), 1.940/1.666 Å (Fe), 1.872/1.714 Å (Co), 1.968/1.789 Å (Ni), 1.999/1.902 Å (Cu) respectively while O1-O2 bond length increases 1.462/1.613 Å (Cr), 1.454/1.856 Å (Mn), 1.463/1.902 Å (Fe), 1.437/1.938 Å (Co), 1.457/2.065 Å (Ni) and 1.427/1.911 Å (Cu) species respectively. These bond parameters support the formation of transition state during O---O bond cleavage. Computed spin density at metal center decreases during O---O bond cleavage i.e. 3.005/1.089 (Cr), 3.831/3.301 (Mn), 3.926/2.826 (Fe), 1.719/2.107 (Co), 1.640/0.929 (Ni), 0.494/0 (Cu). During the O---O bond cleavage with Cu, we have found that buea geometry gets distorted.

As Cu(III) has d^8 electronic configuration with the copper hydroperoxo species,[68] but during O---O bond cleavage electronic configuration at copper center changes i.e. one extra upcoming electron will enter into d_z^2 orbital, which has much higher energy than the d_{xy/x^2-y^2} orbitals due to which during O---O bond cleavage geometry of buea ligand gets distorted. This distortion in geometry may be also due to the John-Teller distortion in Cu d_{xz}/d_{yz} being orthogonal to M-O bond and they can have four electrons in these nonbonding orbitals.

Similar to TMC species, here we have also found that the barrier height of O---O cleavage of Co, Ni, and Cu are relatively higher as compared to corresponding Cr, Mn, and Fe species. This may be due presence of large *d-d* exchange interaction in Cr, Mn, Fe species than the Co, Ni, and Cu species (see Figure 6.14, and 6.15).

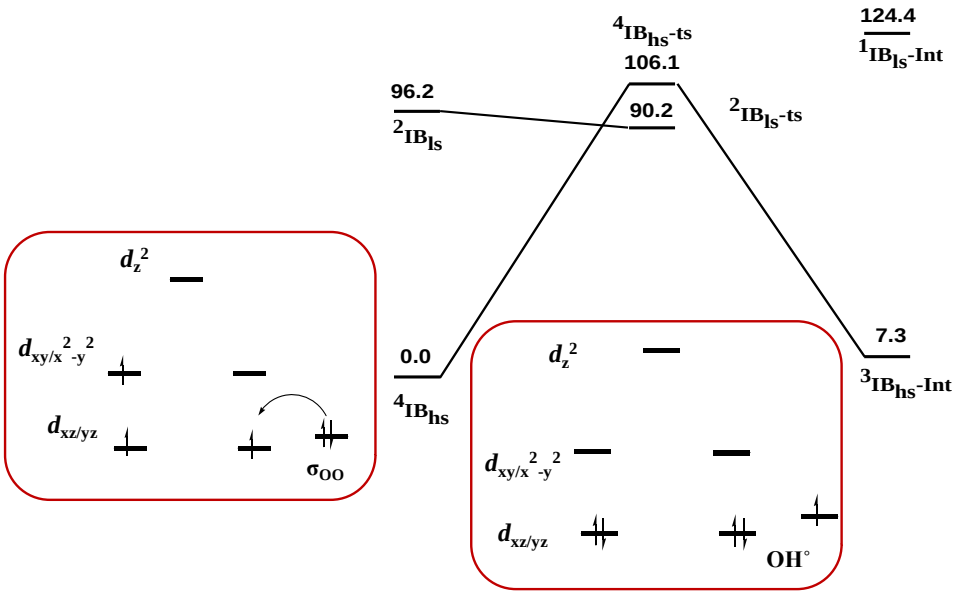

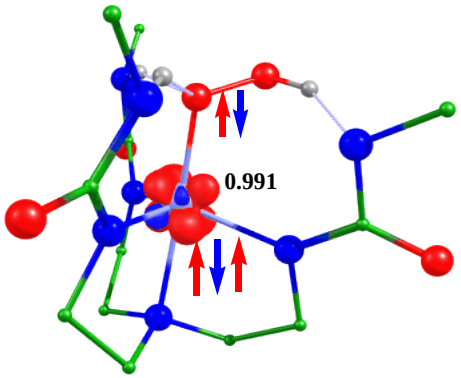

($^2IB_{ls}$)

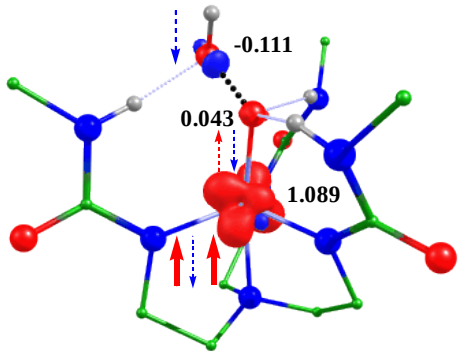

($^2IB_{ls}$-ts)

Figure 6.14. B3LYP-D2 computed energy for the O-O bond cleavage of IB species. The computed barrier height is shown concerning the reactant (IB).

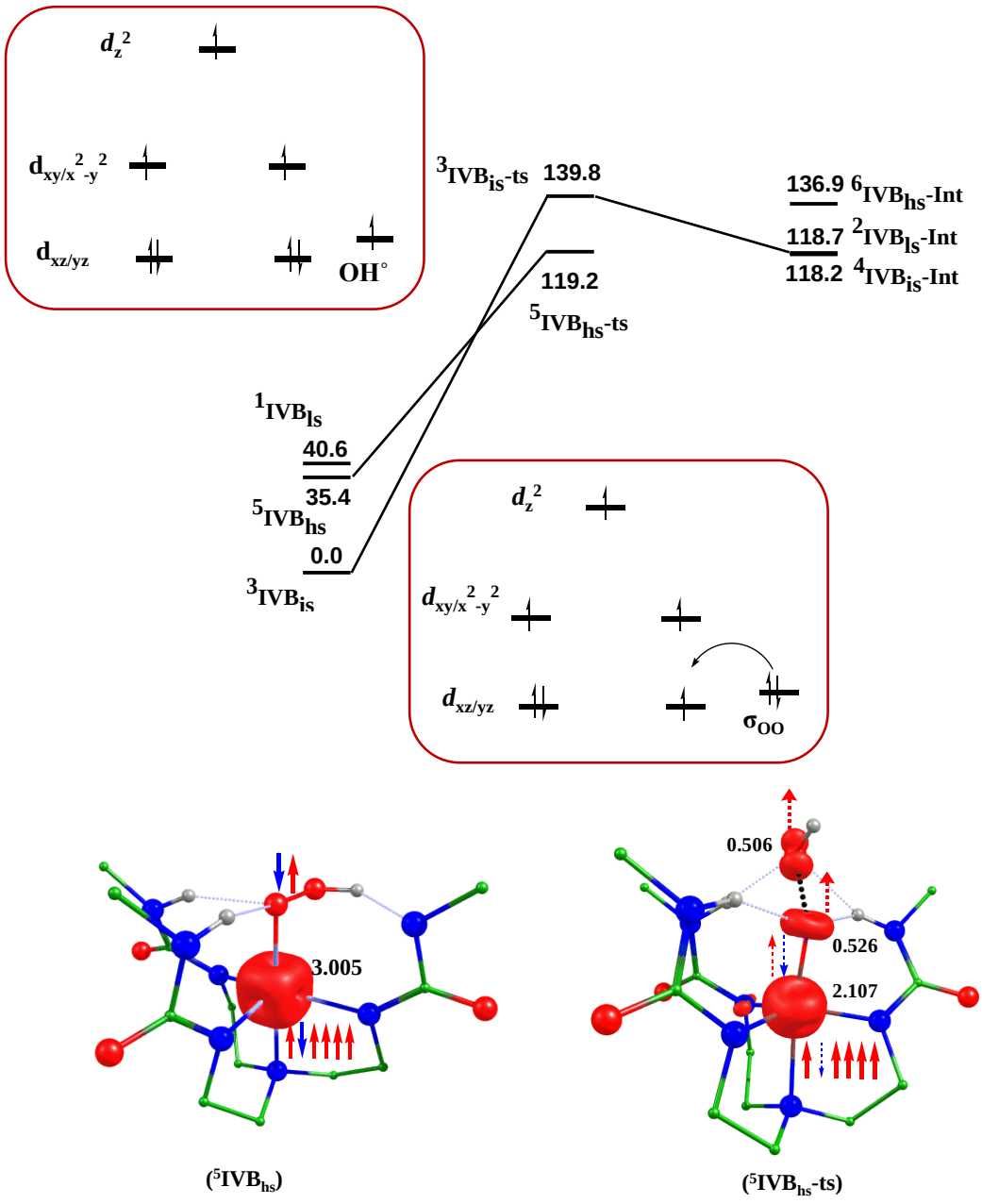

Figure 6.15. B3LYP-D2 computed energy for the O-O bond cleavage of IVB species. The computed barrier height is shown with respect to the reactant (IVB).

The spin natural orbital with occupancies of orbital of ground state of IB, IIB, IIIB, IVB, VB and VIB species and their corresponding O---O bond cleavage transition states are shown in Figure 6.16 these shows the transfer of electron during O---O bond cleavage. Computed wiberg bond index also shows the formation of O---O bond cleavage transition state (see

Table AX 6.4 of appendix). As buea has trigonal bipyramidal geometry and the splitting of *d* orbital is supported by CFT is like $d_{xz} \approx d_{yz} < d_{xy} \approx d_{x^2-y^2} < d_{z^2}$ as shown in Figure 6.17, d_{z^2} orbital have the highest energy and is also supported by Ray (see Figure 6.17). Computed electronic configuration at IB and IIB are found to be $(d_{xz})^1 (d_{yz})^1 (d_{xy})^1 (d_{x^2-y^2})^0 (d_{z^2})^0$ and $(d_{xz})^1 (d_{yz})^1 (d_{xy})^1 (d_{x^2-y^2})^1 (d_{z^2})^0$ (see Figure 6.17). O---O bond cleavage leads to the formation of metal-oxo species. We have performed calculation on all possible electronic configuration of metal-oxo species from the spin energetics it is found that $^3IB_{hs}$-Int, $^4IIB_{hs}$-Int, $^5IIIB_{hs}$-Int, $^5IIIB_{hs}$-ts, $^4IVB_{is}$-Int, $^5VB_{hs}$-Int and $^4VIB_{hs}$-Int are the ground state. Selected bond parameters of metal-oxo species are shown in Table AX 6.3 of appendix. Selected spin density are shown in Table 6.3. Optimized structure and spin density plots of ground state are shown in Figure 6.18. A significant electron densiy at the metal-oxo, oxygen atom indicates its reactive nature.

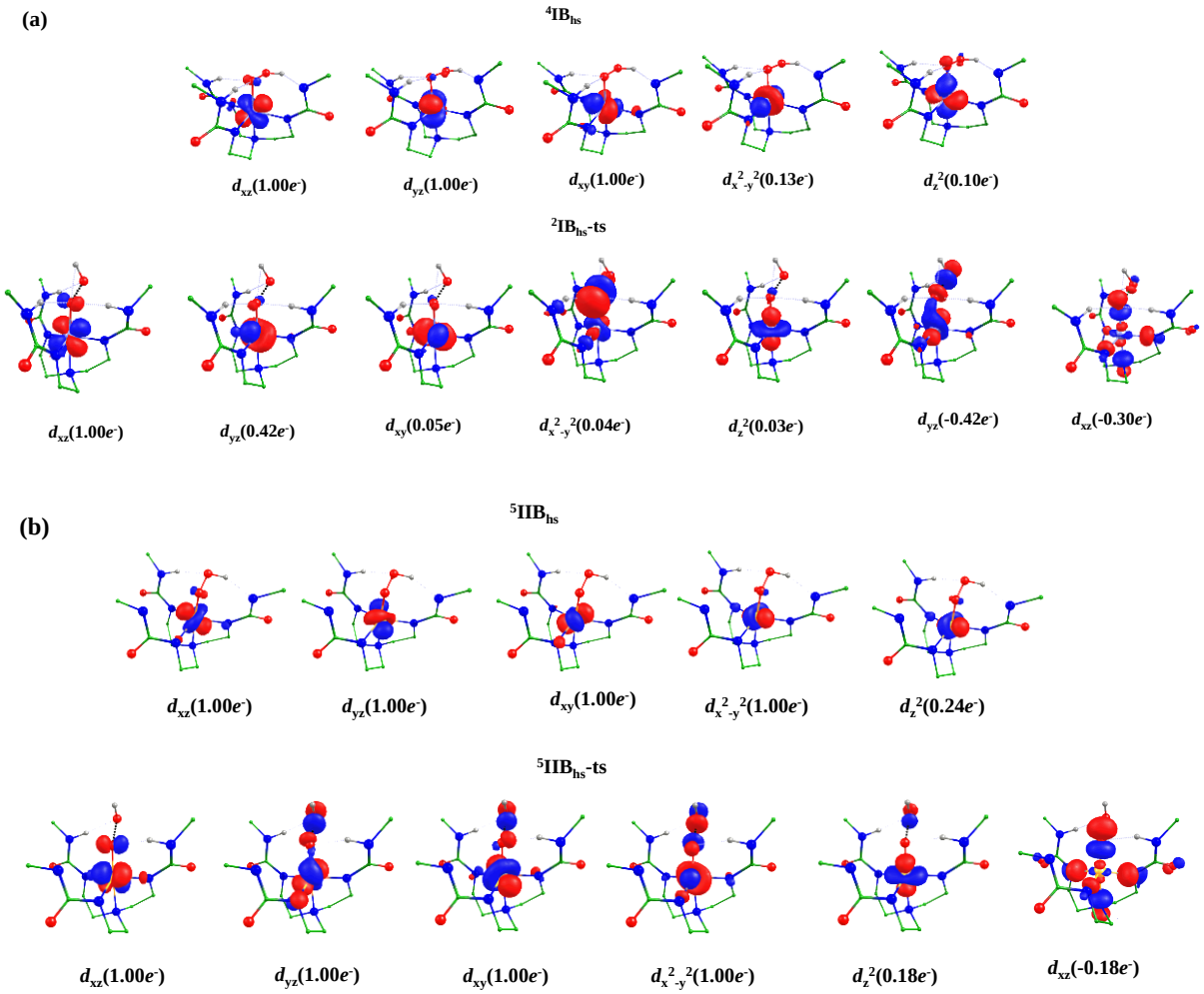

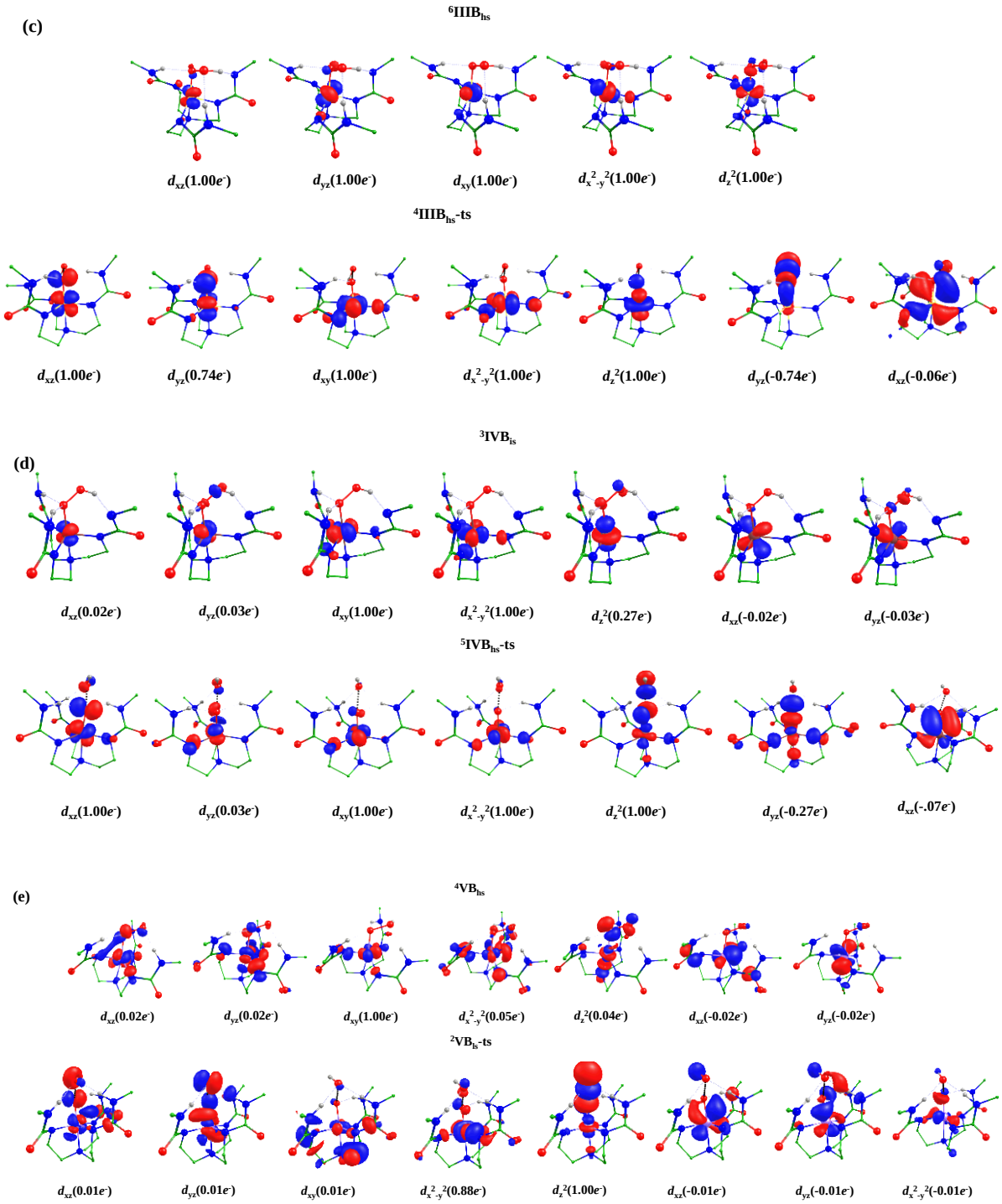

Figure 6.16. Spin natural orbitals and their occupations (noted in parenthesis) of a) ^{2}IB$_{ls}$, ^{2}IB$_{hs}$-ts, b) ^{5}IIB$_{hs}$, ^{5}IIB$_{hs}$-ts, c) ^{6}IIIB$_{hs}$, ^{4}IIIB$_{is}$-ts, d) ^{3}IVB$_{is}$, ^{5}IVB$_{hs}$-ts, e) ^{4}VB$_{hs}$, ^{2}VB$_{ls}$-ts.

Computed stretching frequency of ground state of metal-oxo species are shown in Table 6.2. From literature, only one Co^{IV}=O species with TBP geometry, where oxo is attached to Lewis acid additionally is reported yet.[71] Along with these species, we have also performed

calculation on Ru (VIIB), Os (VIIIB), Rh (IXB), and Ir (XB). We have optimized all the possible electronic configuration of species VIIB, VIIIB, IXB and XB and computed the barrier height of O---O bond cleavage with Ru (VIIB), Os (VIIIB), Rh (IXB), and Ir (XB) with buea ligand. Fom the calculation it is found that $^{2}VIIB_{hs}$, $^{2}VIIIB_{hs}$, $^{1}IXB_{hs}$, and $^{1}XB_{is}$ spin states are the ground state. Selected bond parameters of ground state are shown in Table AX 6.5 of appendix. Optimized structure of ground of species VIIB, VIIIB, IXB and XB are shown in Figure 6.19a,c,e,g. It is found that the O---O bond cleavage barrier is higher with Rh (111.8 kJ/mol; $^{3}IXB_{hs}$-ts) and Ir (77.3 kJ/mol; $^{1}XB_{is}$-ts) species than the corresponding Ru (52.7 kJ/mol; $^{2}VIIB_{ls}$-ts) and Os (21.2 kJ/mol; $^{2}VIIIB_{hs}$-ts) species. We tired to compute transition state of O---O bond cleavage at other spin surfaces of VIIB, VIIIB, IXB and XB species but we were not able to compute all these due to convergence issue. We also tried to compute the barrier height of O---O bond cleavage with 14-TMC and computed the barrier height of O---O bond cleavage with Ru (49.7 kJ/mol) but not be able to compute the barrier with Os, Rh and Ir due to convergence issue. The Optimized ground state structure of VIIB-ts, VIIIB-ts, IXB-ts and XB-ts are shown in Figure 6.19(b,d,f,h).

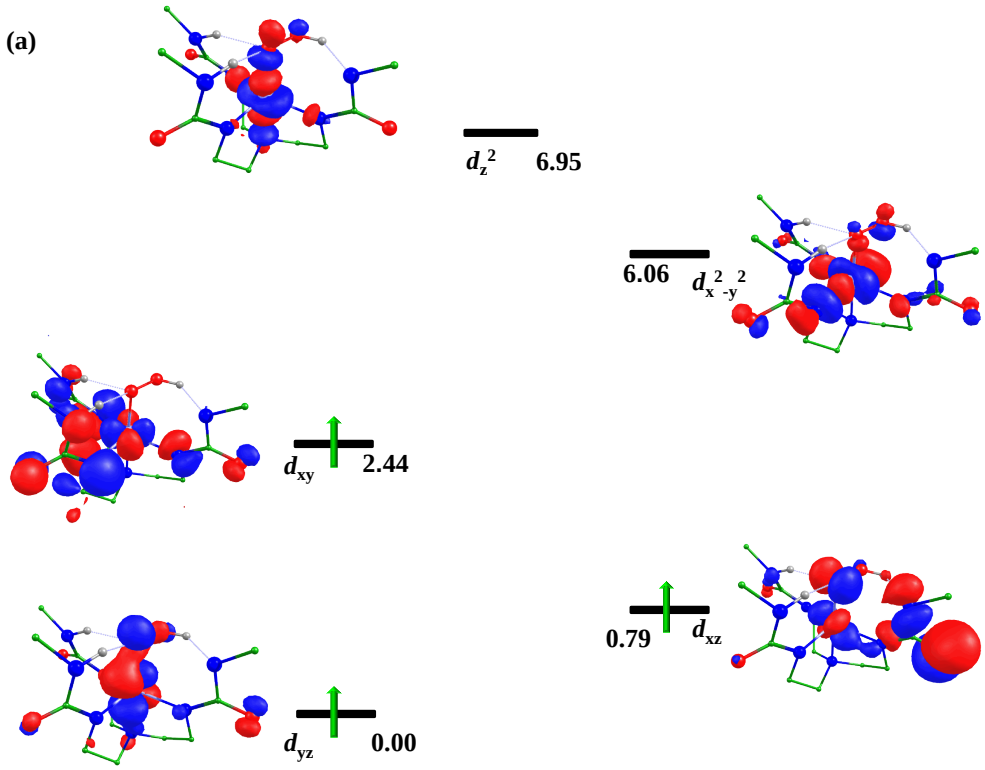

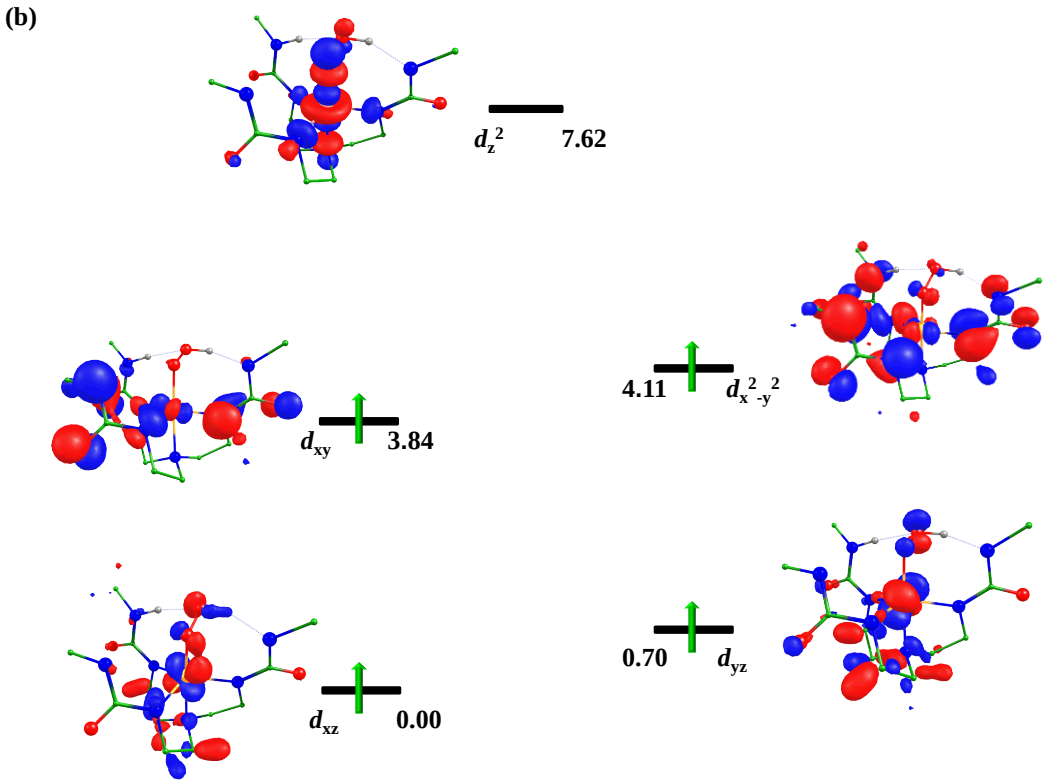

Figure 6.17. Computed eigenvalue plot incorporating energies computed for *d*-based orbitals for alpha and beta spin corresponding to the ground state $^{4}IB_{hs}$, $^{5}IIB_{hs}$ of the complex IIB (energies are given in eV).

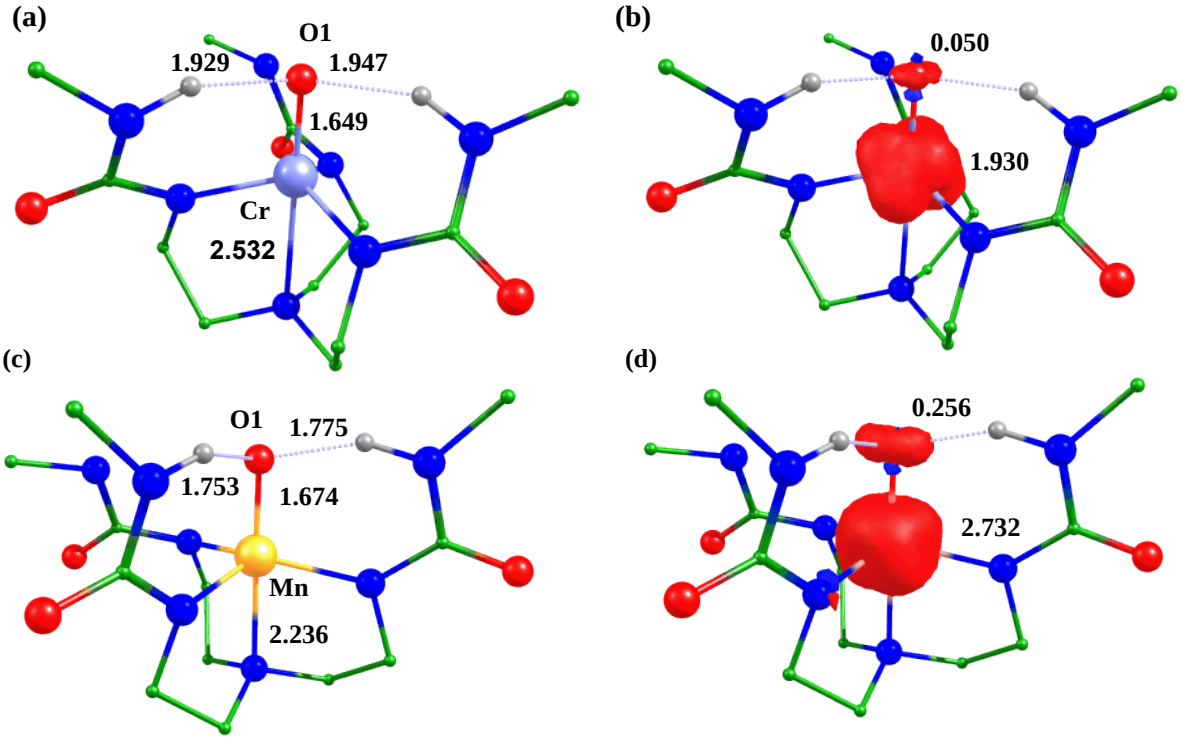

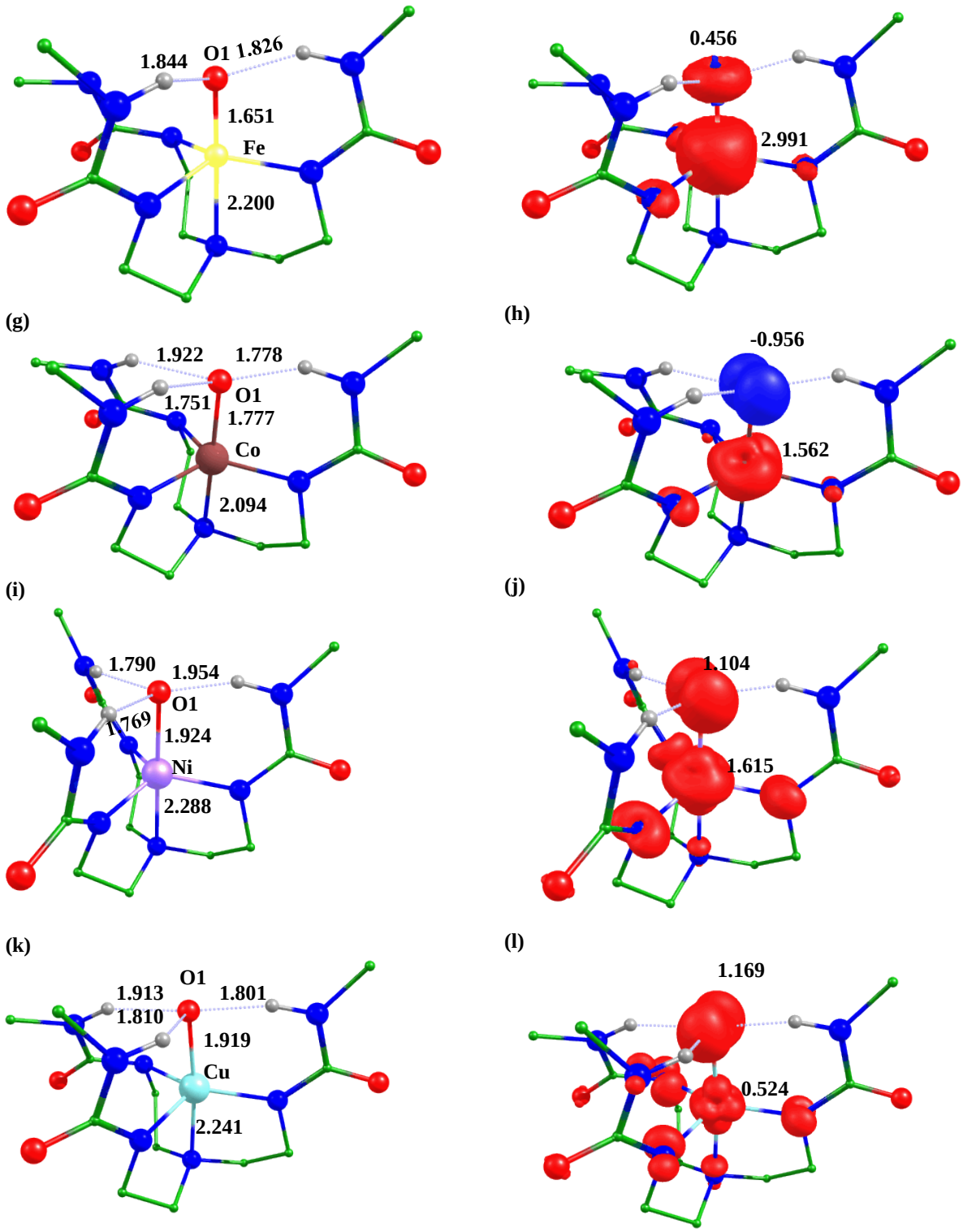

Figure 6.18. B3LYP-D2 a) optimized structure (bond length in Å) b) spin density plot of $^{3}IB_{hs}$-Int; c) optimized structure (bond length in Å) d) spin density plot of $^{4}IIB_{hs}$-Int; e) optimized structure (bond length in Å) f) spin density plot of $^{5}IIIB_{hs}$-Int and $^{5}IIIB_{hs}$-ts; g) optimized structure (bond length in Å) h) spin density plot of $^{4}IVB_{is}$-Int; i) optimized

structure (bond length in Å) j) spin density plot of $^{5}VB_{hs}$-Int; k) optimized structure (bond length in Å) and l) spin density plot of $^{4}VIB_{hs}$-Int.

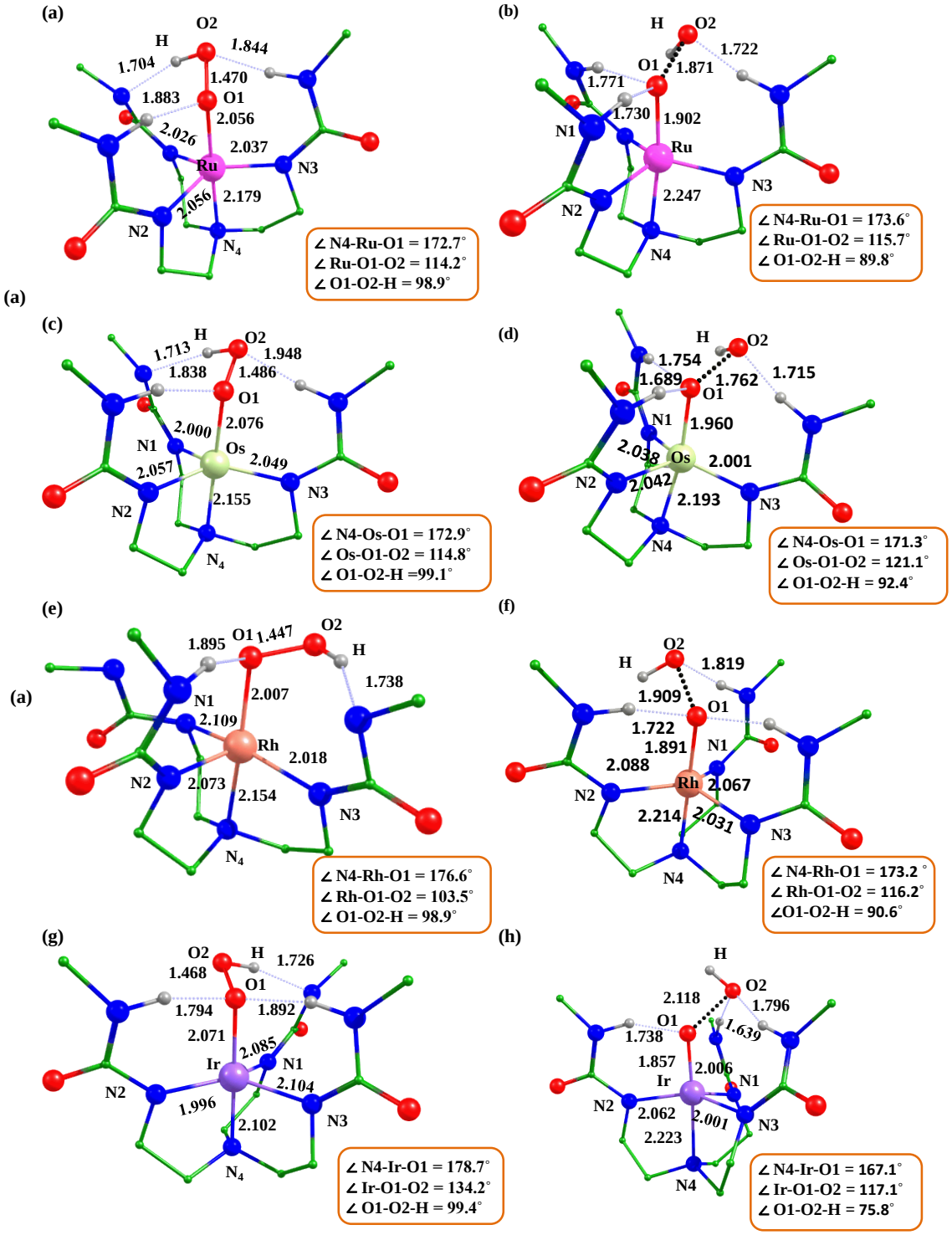

Figure 6.19. B3LYP-D2 optimized structure of ground state $^{2}VIIB_{hs}$, $^{2}VIIIB_{hs}$, $^{1}IXB_{hs}$, $^{1}XB_{is,}$ and $^{4}VB_{hs,}$ and their corresponding transition states $^{2}VIIB_{ls}$-ts, $^{2}VIIIB_{hs}$-ts, $^{3}IXB_{hs}$-ts, $^{1}XB_{is}$-ts.

6.3.3 Comparative study

Computed O---O bond cleavage barrier heights are relatively higher with Co, Ni, and Cu hydroperoxo species than the Cr, Mn, and Fe species. This higher barrier height with (Co, Ni, Cu) species may be due to the pairing of β-electron in the *d*-orbital which decreases the *d*-*d* exchange interaction due to which electronic repulsion increases, which increases the O---O bond cleavage barrier height. Earlier Cr, Mn, Fe species have more number of unpaired electrons as compared to Co, Ni, and Cu species due to which earlier hydroperoxo species (Cr, Mn, Fe) have smaller barrier height of O---O bond cleavage due to enhanced exchange reactivity, which states more the number of unpaired electron more will be the reactivity.[73] Along with this, we saw that filling of an electron in antibonding orbitals starts after d^6 electronic configuration, and due to occupancy of an electron in antibonding orbital decreases bond order which is computed by wiberg bond index, which in turn increases the barrier for O---O bond cleavage. After the O---O bond cleavage metal-oxo species with $OH^{\cdot}/OH^{-}$ are formed, we have computed the energties of these species also. Energy of *d* orbital depends upon the effective nuclear charge on metal, as on going from left to right in periodic table, energy of metal *d* orbitals decreases with increase in the oxidation state of metal. As in early transition metals *d* orbitals are at a higher energy level than the filled O (2*p*) orbital. Due to a decrease in metal *d* orbital energy, this results in incomparable energy of metal *d* orbital and O (2*p*) orbital. From, the computed energies we have found that the energies of metal-oxo (Co-O, Ni-O, and Cu-O) are much higher than that of metal-oxo of Cr-O, Mn-O, and Fe-O with both the 14-TMC and buea ligand (see Figure 6.20). This indicates the instability of late transition metal-oxo species. From, the Computed structural parameters (see Table AX 6.1 and Table AX 6.3 of appendix), we have found that Co-O, Ni-O, and Cu-O bond lengths are longer than the normal metal-oxo bond length with both 14-TMC and buea ligands, and these

long bond lengths are supported by computed smaller metal-oxo (Co-O, Ni-O, and Cu-O) vibrational frequencies (see Table 6.2).

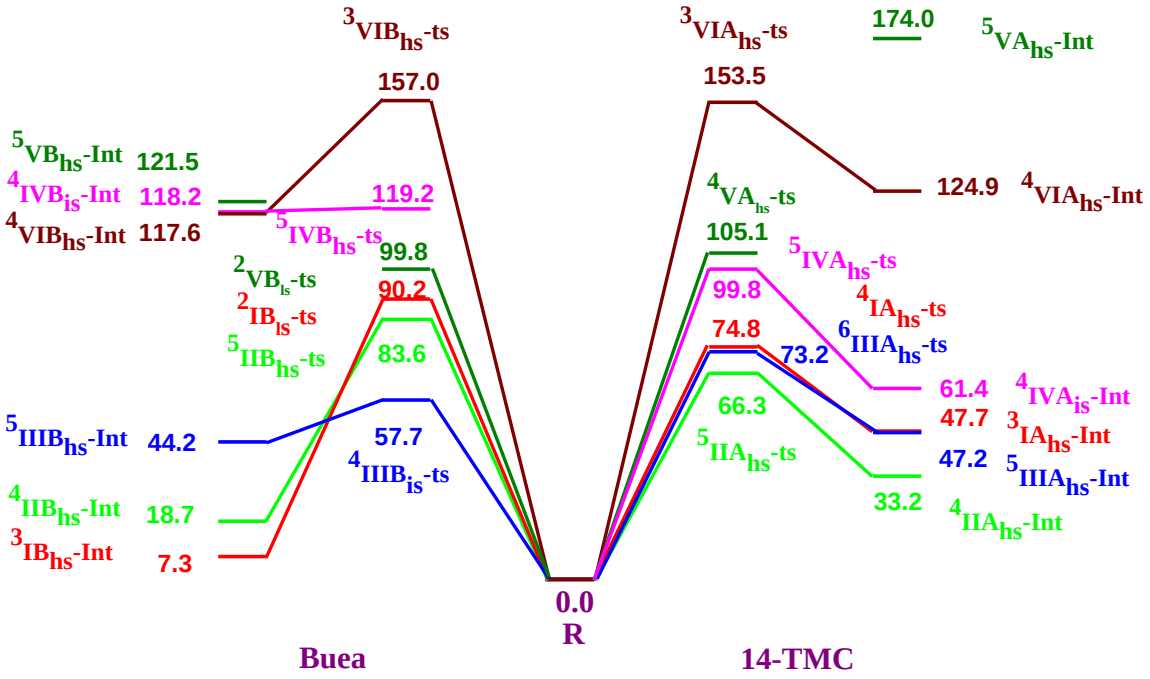

Figure 6.20. B3LYP-D2 computed energy surface for the formation of metal-oxo from metalhydroperoxo with 14-TMC and buea ligand.

Cobalt-oxo bond length is longer also supported by the experiment results.[73-75] These data indicates that the late transition metal-oxo bond has a single bond character. Spin densities at oxygen in metal-oxo (Co, Ni, and Cu) are 0.884/0.664, 1.571/1.104, and 1.362/1.169 with TMC and buea ligand respectively. Metal-oxo bond length and the spin densities at metal and oxygen atoms of metal-oxo show that there exists the valence tautomerism between metal and oxygen.[76] All these support the formation of metal-oxyl and its reactive nature. Intramolecular H-bonding is present in the buea ligand which stabilizes the molecule (see Figure 6.18 and 6.20) that the energy of metal-oxo species formed after O---O bond cleavage with buea ligand has smaller energy as compared to metal-oxo species formed with 14-TMC ligand except for Co^{IV}=O. DFT calculations have been also performed for the formation of terminal metal-oxo species of first the two different ligands.

6.4 Conclusions

From our DFT calculations, we have predicted that O---O bond cleavage in metal hydroperoxo species occurs homolytically and the barrier for O---O cleavage are higher with the late transition metal hydroperoxo species (Co, Ni, Cu) than that of earlier metal-hydroperoxo species (Cr, Mn, Fe) in both the geometries, this higher barrier height of late transition metals (Co, Ni, and Cu) species may be because the pairing of the electron in *d* orbital of metals starts due to which the *d-d* electron exchange interactions decreases due to which the electron-electron repulsion gets dominated which increases the O---O bond cleavage which in turn decreases the stability of metal-oxo. In the earlier transition metal, there are vacant orbital present due to which they can easily accept the electrons donated by oxygen and can easily form the π bond while in the late transition metals there exist the repulsion between the metal filled *d*-orbital electrons and the electron donated by an oxygen atom and thus they do not form the π bond easily. This is also supported in Ru, Rh, Os, and Ir hydroperoxo species. Transition metals from Cr to Cu hydroperoxo species, the computed energies, we have found that metal-oxo of Co, Ni, and Cu are relatively at higher energy than that of Cr, Mn, and Fe oxo species. From, the computed structural parameter of metal-oxo and spin density at metal and oxygen atom suggests that valence tautomerism exists between metal and oxygen in late transition metal-oxo species (Co, Ni, and Cu). Thus, we can say that the metal-oxo of the late transition metal series exists as metal-oxyl. Metal-oxo species acts as a reactive intermediate in the oxidation reaction, along with these are also involved in O-O bond formation. The formation of metal-oxyl seems to be important for O-O coupling.

Their convincing evidence are available for the involvement of these reactive intermediates in many metal-mediated catalytic nucleophilic and electrophilic reactions which are familiar in

biology and chemistry. The study of these species with structure and function relations may lead to a general system that functionalizes the C-H bond or carry group transfer reactions.